Outflows from super star clusters in the central starburst of NGC 253

Levy, R.C.; Bolatto, A.D.; Leroy, A.K.; Emig, K.L.; Gorski, M.; Krieger, N.; ... ; Zwaan, M.A.

DRAFT VERSION NOVEMBER 12, 2021
Typeset using LaTeX **twocolumn** style in AASTeX63

Outflows from Super Star Clusters in the Central Starburst of NGC 253

REBECCA C. LEVY,[1] ALBERTO D. BOLATTO,[1] ADAM K. LEROY,[2] KIMBERLY L. EMIG,[3] MARK GORSKI,[4] NICO KRIEGER,[5] LAURA LENKIĆ,[1] DAVID S. MEIER,[6,7] ELISABETH A. C. MILLS,[8] JÜRGEN OTT,[7] ERIK ROSOLOWSKY,[9] ELIZABETH TARANTINO,[1] SYLVAIN VEILLEUX,[1] FABIAN WALTER,[5,7] AXEL WEIß,[10] AND MARTIN A. ZWAAN[11]

[1]*Department of Astronomy, University of Maryland, College Park, MD 20742, USA*
[2]*Department of Astronomy, The Ohio State University, Columbus, OH 43210, USA*
[3]*Leiden Observatory, Leiden University, PO Box 9513, 2300-RA Leiden, the Netherlands*
[4]*Chalmers University of Technology, Gothenburg, Sweden*
[5]*Max-Planck-Institut für Astronomie, Königstuhl 17, 69120 Heidelberg, Germany*
[6]*Department of Physics, New Mexico Institute of Mining and Technology, 801 Leroy Pl., Socorro, NM, 87801, USA*
[7]*National Radio Astronomy Observatory, P. O. Box O, 1003 Lopezville Rd., Socorro, NM, 87801, USA*
[8]*Department of Physics and Astronomy, University of Kansas, 1251 Wescoe Hall Dr., Lawrence, KS 66045, USA*
[9]*Department of Physics, University of Alberta, 4-183 CCIS, Edmonton, Alberta, T6G 2E1, Canada*
[10]*Max-Planck-Institut für Radioastronomie, Auf dem Hügel 69, D-53121 Bonn, Germany*
[11]*European Southern Observatory, Karl-Schwarzschildstrasse 2, D-85748 Garching Bei Muenchen, Germany*

ABSTRACT

Young massive clusters play an important role in the evolution of their host galaxies, and feedback from the high-mass stars in these clusters can have profound effects on the surrounding interstellar medium. The nuclear starburst in the nearby galaxy NGC 253 at a distance of 3.5 Mpc is a key laboratory in which to study star formation in an extreme environment. Previous high resolution (1.9 pc) dust continuum observations from ALMA discovered 14 compact, massive super star clusters (SSCs) still in formation. We present here ALMA data at 350 GHz with 28 milliarcsecond (0.5 pc) resolution. We detect blueshifted absorption and redshifted emission (P-Cygni profiles) towards three of these SSCs in multiple lines, including CS 7–6 and $H^{13}CN$ 4–3, which represents direct evidence for previously unobserved outflows. The mass contained in these outflows is a significant fraction of the cluster gas masses, which suggests we are witnessing a short but important phase. Further evidence of this is the finding of a molecular shell around the only SSC visible at near-IR wavelengths. We model the P-Cygni line profiles to constrain the outflow geometry, finding that the outflows must be nearly spherical. Through a comparison of the outflow properties with predictions from simulations, we find that none of the available mechanisms completely explains the observations, although dust-reprocessed radiation pressure and O star stellar winds are the most likely candidates. The observed outflows will have a very substantial effect on the clusters' evolution and star formation efficiency.

Keywords: galaxies: individual (NGC 253) — galaxies: starburst — galaxies: star clusters — ISM: kinematics — ISM: molecules

1. INTRODUCTION

Many stages of the stellar life cycle inject energy and momentum into the surrounding medium. For young clusters of stars, this feedback can alter the properties of the cluster itself in addition to the host galaxy. Outflows from young clusters, in particular, remove gas that may have otherwise formed more stars, affecting the star formation efficiency (SFE) of the cluster. The gas clearing process can proceed through a number of physical mechanisms that are efficient over different density regimes and timescales, such as photoionization, radiation pressure, supernovae, and stellar winds. Outflows from forming massive clusters have been observed in the Large Magellanic Cloud (Nayak et al. 2019) and in the Antennae (Gilbert & Graham 2007; Herrera & Boulanger 2017).

At high levels of star formation, a larger fraction of stars form in clustered environments (Kruijssen 2012; Johnson et al. 2016; Ginsburg & Kruijssen 2018). The most extreme star forming environments can lead to massive ($M_* > 10^5$

Corresponding author: Rebecca C. Levy
rlevy@astro.umd.com

$M_\odot$) and compact (r $\sim$ 1 pc) so-called "super" star clusters (SSCs; e.g., Portegies Zwart et al. 2010). Because they are often deeply embedded, observations of young SSCs in the process of forming are rare (Herrera & Boulanger 2017; Oey et al. 2017; Turner et al. 2017; Leroy et al. 2018; Emig et al. 2020). Observations and simulations both indicate that SSCs should have high SFEs (e.g., Skinner & Ostriker 2015; Oey et al. 2017; Turner et al. 2017; Krumholz et al. 2019, L. Lancaster et al., in prep.). Given these high SFEs, by what process(es) do these SSCs disperse their natal gas?

NGC 253 is an ideal target to study massive, clustered star formation in detail. It is one of the nearest (d$\sim$3.5 Mpc; Rekola et al. 2005) starburst galaxies forming stars at a rate of $\sim$2 $M_\odot$ yr^{-1} in the central kiloparsec (Bendo et al. 2015; Leroy et al. 2015). The star formation is concentrated in dense clumps, knots, and clouds of gas (Turner & Ho 1985; Ulvestad & Antonucci 1997; Paglione et al. 2004; Sakamoto et al. 2006, 2011; Bendo et al. 2015; Leroy et al. 2015; Ando et al. 2017). Recent high-resolution data from the Atacama Large Millimeter/submillimeter Array (ALMA) reveal at least 14 dusty, massive proto-SSCs (Leroy et al. 2018) at the heart of these larger dense gas structures. Moreover, the clusters themselves have radio recombination line (RRL) and radio continuum emission (E. A. C. Mills et al. in prep.), further confirmation that these are young clusters.

However, even at the 1.9 pc ($0.11''$) resolution of the previous study by Leroy et al. (2018), the clusters, which have radii of $0.6-1.5$ pc, are only marginally resolved. Even higher resolution data are needed to spatially resolve these compact clusters to study the cluster-scale kinematics and feedback.

Here we present direct evidence for massive outflows from three forming SSCs in the center of NGC 253 using new, very high resolution ($0.028'' \approx 0.48$ pc $\approx 10^5$ AU) data from ALMA at 350 GHz. These three clusters show blueshifted absorption and redshifted emission line profiles—P-Cygni profiles—in several lines. Our analysis shows that these profiles are a direct signature of massive outflows from these SSCs. We briefly describe the observations, data processing, and imaging in Section 2. We present measured properties of the outflows from three SSCs based on the line profiles and modeling in Section 3. We discuss the relevant timescales of the outflows and clusters in terms of their evolutionary stage, mechanisms to power the outflows, and comment on the specific case of SSC 5—which is the only cluster visible in the NIR—in Section 4. We summarize our findings in Section 5.

The analysis in this paper will be focused on the three clusters with clear P-Cygni profiles: SSCs 4a, 5a, and 14. We will focus on results obtained from the CS $7-6$ and H^{13}CN $4-3$ lines for the following reasons. First, these lines show bright emission towards many of the SSCs and are detected at relatively high signal-to-noise ratio (SNR). Because of their high critical densities ($n_{\rm crit}\sim 3-5\times10^6$ cm^{-3} and $n_{\rm crit}\sim 0.8-2\times10^7$ cm^{-3} respectively; Shirley 2015) they probe gas that is more localized to the clusters themselves, lessening uncertainties introduced by the foreground gas correction (Section 2.4). In the case of H^{13}CN $4-3$, the ^{13}C/^{12}C isotopic ratio means this line is even less likely to be very optically thick. Although strong, the CO $3-2$ line shape is complicated because it has components from clouds along the line of sight that are not associated with the clusters. Though the HCN $4-3$ and HCO$^+$ $4-3$ lines are bright and also have high critical densities ($n_{\rm crit}\sim 0.9-3\times10^7$ cm^{-3} and $n_{\rm crit}\sim 2-3.6\times10^6$ cm^{-3} respectively; Shirley 2015), they are more abundant and more optically thick than CS $7-6$ and H^{13}CN $4-3$, and the absorption components in these lines suffer from saturation (i.e. absorption down to zero). This makes determining physical quantities of the outflows—which rely on the absorption depth to continuum ratio (Section 3)—difficult and uncertain. Therefore, we find that the CS $7-6$ and H^{13}CN $4-3$ lines provide the best balance between bright lines with sufficient SNR, absorption features which do not suffer from saturation effects, and which probe gas localized to the clusters to minimize uncertainties from the foreground gas correction.

2. OBSERVATIONS, DATA PROCESSING, AND OUTFLOW IDENTIFICATION

Data for this project were taken with the Atacama Large Millimeter/submillimeter Array (ALMA) as part of project 2017.1.00433.S (P.I. A. Bolatto). We observed the central $16.64''$ (280 pc) of NGC 253 at Band 7 ($\nu\sim350$ GHz, $\lambda\sim0.85$ μm) using the main 12-m array in the C43-9 configuration. The spectral setup is identical to our previous observations of this region (Leroy et al. 2018; Krieger et al. 2019, 2020), spanning frequency ranges of $342.08-345.78$ GHz in the lower sideband and $353.95-357.66$ GHz in the upper sideband. Observations were taken on November $9-11$, 2017 with a total observing time of 5.7 hours of which 2.0 hours were on-source. The visibilities were pipeline calibrated using the Common Astronomy Software Application (CASA; McMullin et al. 2007) version 5.1.1-5 (L. Davis et al. in prep.). J0038-2459 was the phase calibrator and J0006-0623 was the bandpass and flux calibrator.

2.1. *Imaging the Continuum*

In this paper, we focus on the line profiles, specifically the CS $7-6$ and H^{13}CN $4-3$ lines towards three of the SSCs. We will present the continuum data more fully in a forthcoming paper (R. C. Levy et al., in prep.). Some of the data are presented and used here, and we provide a brief summary. To extract the 350 GHz continuum data, we flagged spectral windows that may contain strong lines in the band, assuming a systemic velocity of 243 km s^{-1} (Koribalski et al. 2004). We imaged the line-flagged cube with 5 km s^{-1} channels using the CASA version 5.4.1 `tclean` task with `specmode='mfs'`, `deconvolver='multiscale'`, `scales=[0,4,16,64]`, Briggs weighting with `robust=0.5`, and no *uv*-taper. The baseline was fit with two terms to account for any change in slope over the wide band. The continuum was cleaned down to a threshold of 27 μJy beam^{-1}, after which the residuals resembled noise. This map has a beam size of $0.024'' \times 0.016''$ and a cell (pixel) size of $0.0046''$ (0.078 pc), so that we place around 4 pixels across the minor axis of the beam. Finally, the map was convolved to a circular beam size of $0.028''$ (0.48 pc). The rms noise of the continuum image (away from emission) is 26 μJy beam^{-1}(0.3 K).

From this high resolution 350 GHz continuum image (Figure 1), we identify approximately three dozen clumps of dust emission. These are co-spatial with the 14 proto-SSCs identified by Leroy et al. (2018), with many sources breaking apart into smaller clumps that likely represent individual clusters. We follow the SSC naming convention of Leroy et al. (2018), adding letters to denote sub-clusters in decreasing order of brightness. For clusters that break apart, there is always a main, brightest cluster. For example, SSC 4 from Leroy et al. (2018) breaks apart into six dust clumps, where the peak intensity of SSC 4a is $>4\times$ that of any of the smaller clumps. For this paper, we will focus only on the primary clusters since those are the most massive, and smaller dust clumps may not be true clusters. We also remove SSC 6 from this analysis, as it is extended and more tenuous in the high resolution continuum map and so may not be a SSC. Leroy et al. (2018) also note that this clump is weak and may instead be a supernova remnant, which is further supported by a non-trivial synchrotron component to this cluster's spectral energy distribution (SED; E. A. C. Mills et al., in prep.).

The position and orientation of each primary cluster is measured by fitting a 2D Gaussian to each cluster in the continuum image using `emcee` (Foreman-Mackey et al. 2013). The reported values are the medians of the marginalized posterior likelihood distributions (Table 1). As a non-parametric measurement of the cluster sizes, we compute the half-flux radius ($r_{\rm half-flux}$) for each cluster. Given the cluster positions and orientations from the 2D Gaussian fit, we construct elliptical annuli in steps of half the beam FWHM. The half-flux radius is the median of the cumulative flux distribution. We use this radius measurement as opposed to those from the 2D Gaussian fit because the cluster light profiles are not necessarily well described by a Gaussian, which will be discussed further in a forthcoming paper (R. C. Levy et al., in prep.). We deconvolve the beam from the radius measurements by removing half the beam FWHM from the half-flux radius in quadrature. The beam deconvolution—and the fit convergence for the dimmer clusters—will be treated more fully in a forthcoming paper focusing on the continuum properties of the SSCs (R. C. Levy et al., in prep.).

Table 1. Primary Cluster Positions and Sizes Measured from the 350 GHz Continuum Image

SSC Number	R.A. (J2000)	Decl. (J2000)	$r_{\rm half-flux}$ (pc)	$V_{\rm LSRK}$ (km s^{-1})
1a	$0^h47^m32.801^s$	$-25°17'21.236''$	0.59	315
2	$0^h47^m32.819^s$	$-25°17'21.247''$	0.19	305
3a	$0^h47^m32.839^s$	$-25°17'21.122''$	0.47	302
4a	$0^h47^m32.945^s$	$-25°17'20.209''$	0.50	251
5a	$0^h47^m32.987^s$	$-25°17'19.725''$	0.76	215
7a	$0^h47^m33.022^s$	$-25°17'19.086''$	0.59	270
8a	$0^h47^m33.115^s$	$-25°17'17.668''$	1.20	295
9a	$0^h47^m33.116^s$	$-25°17'18.200''$	0.46	155
10a	$0^h47^m33.152^s$	$-25°17'17.134''$	1.32	280
11a	$0^h47^m33.165^s$	$-25°17'17.376''$	0.13	145
12a	$0^h47^m33.182^s$	$-25°17'17.165''$	1.29	160
13a	$0^h47^m33.198^s$	$-25°17'16.750''$	0.36	245
14	$0^h47^m33.297^s$	$-25°17'15.558''$	0.53	205

NOTE—The cluster positions and sizes for the primary SSCs identified from the 350 GHz continuum image (Figure 1). We follow the cluster naming convention of Leroy et al. (2018). Clusters that break apart into multiple sub-clusters have an "a" added to their number. We remove SSC 6 as it is likely not a true cluster due to its morphology. Positions are determined by fitting a 2D Gaussian. $r_{\rm half-flux}$ is the half-flux radius determined from the radial profile. The beam (0.028" = 0.48 pc) has been deconvolved from the reported sizes. $V_{\rm LSRK}$ is the cluster systemic velocity (see Section 2.5). For SSCs 4a, 5, and 14, the estimated uncertainty is ±1 km s^{-1}. For the other clsuters, estimated uncertainties are ±5 km s^{-1}.

2.2. *Imaging the Lines*

We image the CS $7-6$ and $H^{13}CN$ $4-3$ lines by selecting a 800 km s^{-1} window around the line center (rest frequencies of 342.883 GHz and 349.339 GHz respectively), assuming a systemic velocity of 243 km s^{-1} (Koribalski et al. 2004). We clean the lines of interest using `tclean` in CASA version 5.4.1 with `specmode='cube'`, `deconvolver='multiscale'`, `scales = [0]`, Briggs weighting with `robust = 0.5`, and no *uv*-taper. No clean mask was used. The baseline was fit with two terms to account for any change in slope over the wide band. The continuum is not removed from these cubes. The cell (pixel) size is $0.0046''$ (0.078 pc), so that we place around 4 pixels across the minor axis of the beam. The final elliptical beam is $0.027'' \times 0.019''$. Finally, we convolve to a round $0.028''$ (0.48 pc) beam. The rms noise is 0.5 mJy beam^{-1} (6.5 K) per 5 km s^{-1} channel. Figure 2 shows

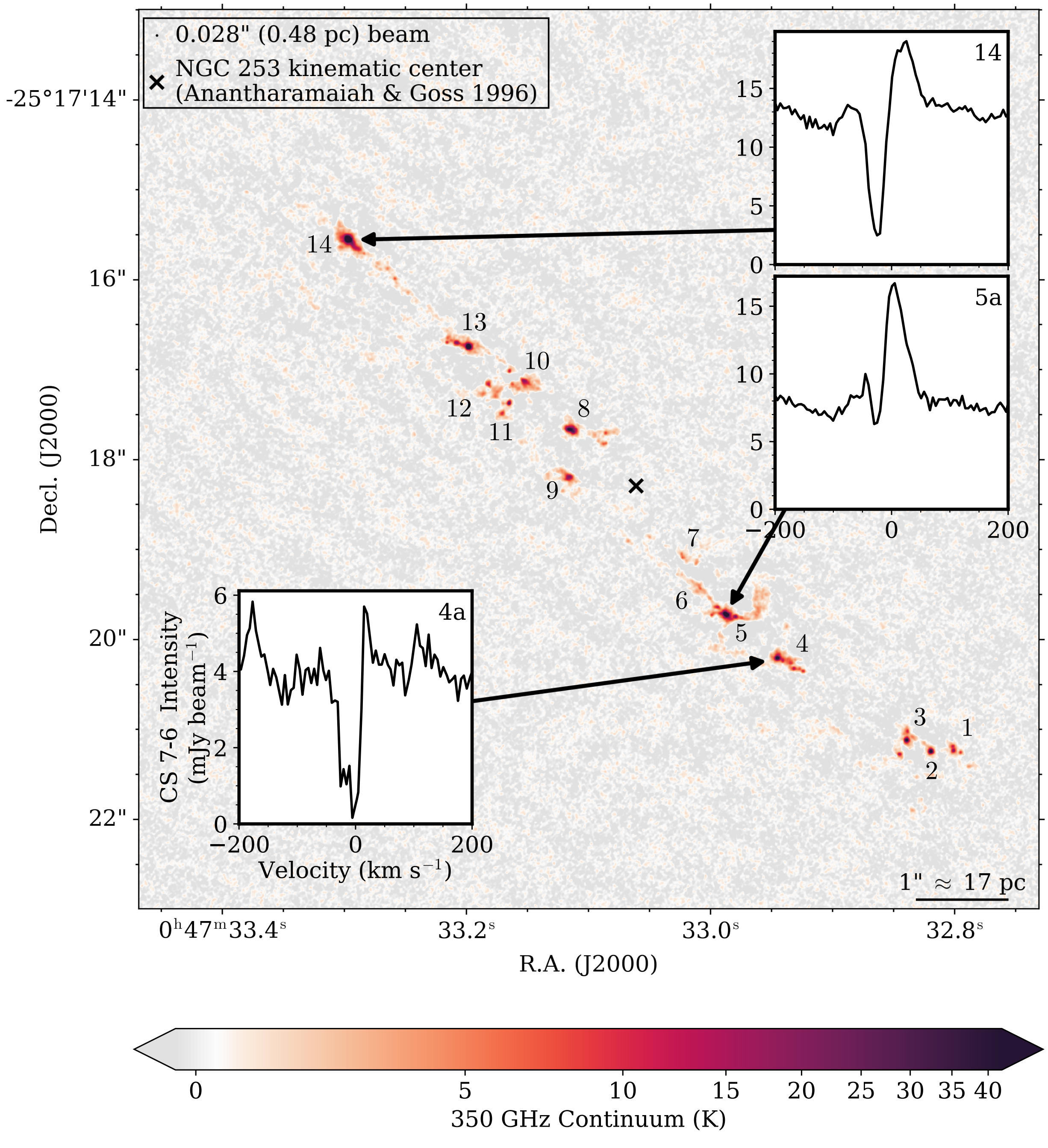

Figure 1. The 350 GHz dust continuum map covering the central $10'' \times 10''$ (170 pc $\times$ 170 pc) of NGC 253 with an rms noise of 26 μJy beam^{-1}(0.3 K). The beam FWHM is shown in the upper left corner. The $\times$ marks the center of NGC 253 from ionized gas kinematics traced by radio recombination lines (Anantharamaiah & Goss 1996). The 14 clusters identified by Leroy et al. (2018) are labeled. Despite the increased resolution most of the massive clusters identified by Leroy et al. (2018) persist, sometimes with a few lower-mass companion objects. The insets show the CS 7−6 spectra towards the three SSCs analyzed in this paper (SSCs 4a, 5a, and 14), highlighting the characteristic P-Cygni profiles indicative of outflows. These are the only clusters toward which we unambiguously identify blueshifted absorption signaling outflow activity.

the peak intensity maps for CS 7−6 and $H^{13}CN$ 4−3 within ± 200 km s^{-1} over the galaxy's systemic velocity to avoid possible contamination by other strong lines (especially by HC_3N in the case of $H^{13}CN$ 4−3).

2.3. *Full-Band Spectra and Detected Lines*

Though the analysis is focused on the CS 7−6 and $H^{13}CN$ 4−3 lines, we also make a "dirty" cube covering the entire band and imaged area by running `tclean` with `niter=0`. This dirty cube has a cell (pixel) size of 0.02″ and an rms noise away from the emitting regions of 0.57 mJy beam^{-1} per 5 km s^{-1} channel. The synthesized beam is 0.05″×0.025″. The continuum is not removed from this cube.

In Figure 3, we show the full band spectrum of SSCs 4a, 5a, and 14, extracted from the dirty cube and averaged over the FWHM continuum source size. There are several immediately striking features in these spectra. The brightest lines in SSCs 4a, 5a, and 14 show deep, blueshifted absorption features, extending down to ~ 0 mJy beam^{-1}. This line profile shape (a P-Cygni profile) is indicative of outflowing material. As a comparison, we also show the spectrum of SSC 8a in Figure 3, which does not have these P-Cygni line shapes. We note that the CO 3−2 line has a complicated structure, likely because it traces lower density gas than other detected lines ($n_{\rm crit} \sim 2\times10^4$ cm^{-3}; e.g., Turner et al. 2017) and so it arises in many places along the line of sight to the SSCs.

There are many detected lines in addition to the usual dense gas tracers. These include shock tracers such as SO 8−7 and SO_2 lines and vibrationally excited HC_3N and HCN 4−3, which are primarily excited through IR pumping (e.g. Ziurys & Turner 1986; Krieger et al. 2020). Many of these have been previously identified by Krieger et al. (2020), some of which are marked in Figure 3.

2.4. *Correcting for Foreground Gas*

Because the SSCs are embedded in the nucleus of NGC 253, there is dense gas along the line of sight which may contribute to the observed spectra but is not associated with the SSCs themselves. This can be seen in the line channel maps around each SSC, shown in Figure 4 for CS 7−6. This gas is most evident in SSCs 5a and 14, which both show changes in the gas morphology with velocity (relative to the cluster systemic velocity; see Section 2.5). The first panel of each set of channel maps shows the CO 3−2 velocity field in the same region as a tracer of the bulk gas motions not associated with the clusters themselves. Because we are interested in the large scale gas motions, we smooth the CO 3−2 velocity maps presented by Krieger et al. (2019) to 5× the beam major axis (5 × 0.17″ = 0.85″ = 14.4 pc). The velocities shown in Figure 4 are relative to the cluster systemic velocities. All three clusters are located at different velocities compared to the bulk gas motions (i.e., CO 3−2 velocity maps are not centered on zero). In the case of SSC 14, the distinct morphological evolution with velocity matches qualitatively with the CO 3−2, though there is a velocity offset. It is difficult to know what fraction of this is associated with the clusters themselves or with dense gas in the environment of the clusters but not necessarily bound to them. Here, we will assume that all of the emission in the green annuli in Figure 4 is not bound to the clusters and should be corrected to obtain the intrinsic spectrum of the clusters. The spectrum of the environmental gas ($T_{\rm env}$) is averaged in an annulus with an inner radius of 3× the half-flux radius and an outer radius of 5× the half-flux radius, as shown in Figure 4. This effectively assumes the environmental dense gas forms a uniform screen in between the cluster and our line of sight. This is unlikely to be the case and is one of the uncertainties of this correction.

We calculate the optical depth (τ_ν) of the environmental gas following Mangum & Shirley (2015). Combining their Equations 24 and 27, we have

$$\tau_\nu = -\ln\left[1 - \frac{\mathrm{k T_{env}}}{\mathrm{h}\nu}\left(\frac{1}{e^{\mathrm{h}\nu/\mathrm{kT_{ex}}}-1} - \frac{1}{e^{\mathrm{h}\nu/\mathrm{kT_{bg}}}-1}\right)^{-1}\right] \quad (1)$$

where the filling fraction is assumed to be unity, the excitation temperature ($T_{\rm ex}$) is 102 ± 28 K and the background temperature ($T_{\rm bg}$) is measured from the continuum level of the environmental spectrum (but is ≈ 0 K). The assumed value of $T_{\rm ex}$ is the average of the excitation temperatures found by Meier et al. (2015) over larger scales in the nucleus (74 K) and by Krieger et al. (2020) for regions more localized to the SSCs (130 K), since the true value of the excitation temperature of this dense gas near the clusters likely falls somewhere between these two measurements. The uncertainty reflects half of the difference of these two values.

We assume that half of the environmental emission comes from the foreground, so that the optical depth of the material along the line of sight in front of the cluster is $\tau_{\nu,\rm fg} = \tau_\nu/2$. We also assume that the environmental gas is colder than the gas in the cluster, so it will absorb emission from the cluster. We then derive the corrected (intrinsic) SSC spectra where

$$\begin{aligned} \mathrm{T_{obs}} &= \mathrm{T_{intrinsic}}\, e^{-\tau_{\nu,\rm fg}} + \mathrm{T_{env}}\,(1-e^{-\tau_{\nu,\rm fg}}) \\ \Rightarrow \mathrm{T_{intrinsic}} &= e^{\tau_{\nu,\rm fg}}\left[\mathrm{T_{obs}} - \mathrm{T_{env}}\,(1-e^{-\tau_{\nu,\rm fg}})\right], \end{aligned} \quad (2)$$

where the second equation is a rearrangement of the first. The observed, environmental, and intrinsic spectra of CS 7−6 for SSCs 4a, 5a, and 14 are shown in Figure 5. This process is repeated for $H^{13}CN$ 4−3 and the full-band spectra in Figure 3. These intrinsic spectra are used throughout the analysis of this paper unless otherwise noted.

As discussed earlier, it is difficult to determine what fraction of the extended emission seen in the channel maps (Figure 4) is environmental or associated with the cluster. More-

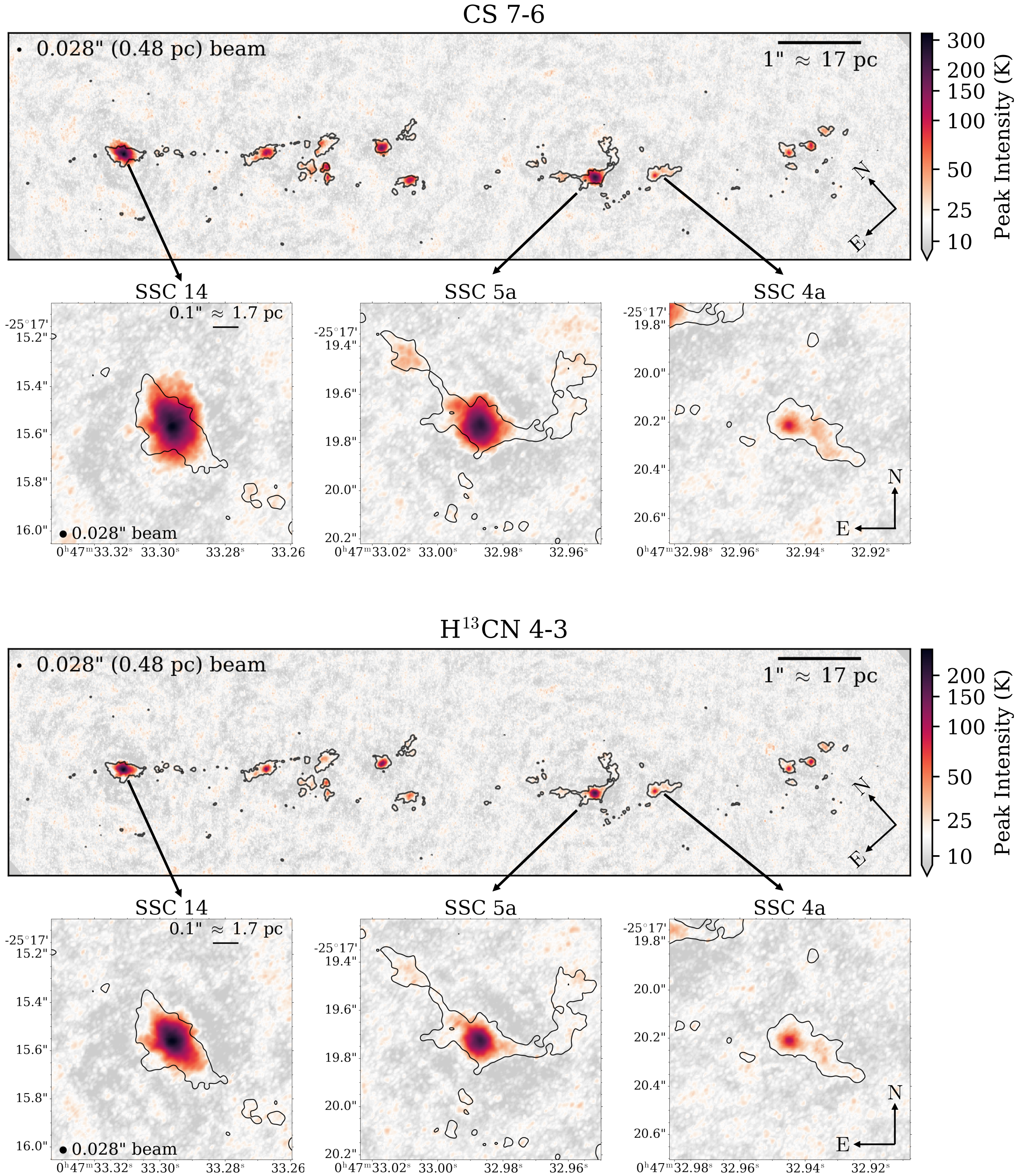

Figure 2. Peak intensity maps of CS 7 – 6 (top group) and $H^{13}CN$ 4 – 3 (bottom group) within ±200 km s^{-1} of the galaxy systemic velocity to avoid contamination by other strong lines in the band. The top panels in each group have been rotated so the linear structure is horizontal, as indicated by the coordinate axes in the lower right corner. The contours show 5 times the rms noise level in the 350 GHz dust continuum shown in Figure 1 (5×rms = 1.5 K), and so indicate the extent of the dust structures around the SSCs. The square plots show the peak intensity maps and dust continuum contours zoomed in to 1″ (17 pc) square regions around SSCs 14, 5a, and 4a, highlighting the localized and spatially resolved emission towards these SSCs. These have not been rotated, as indicated by the coordinate axes in the lower right corner.

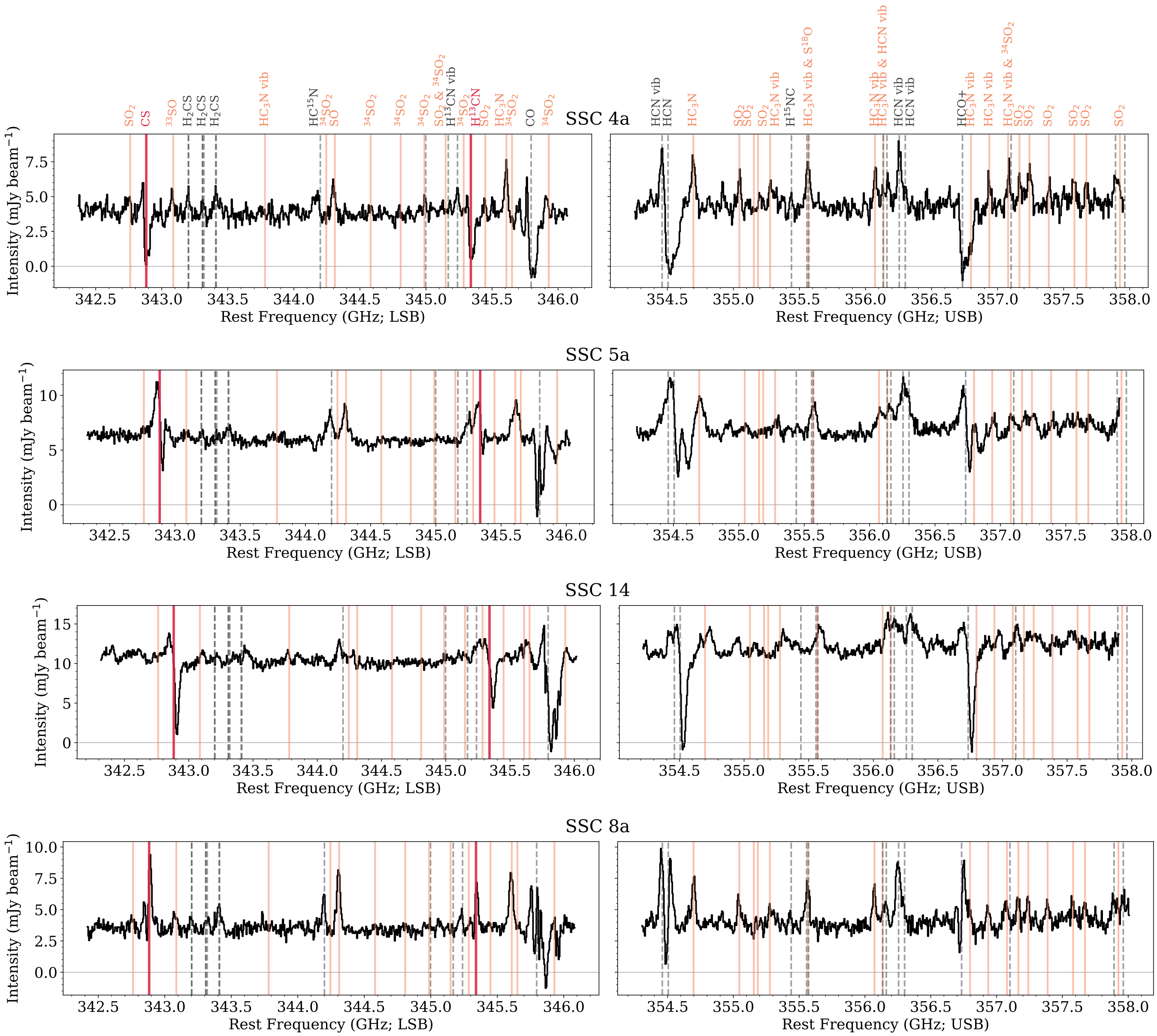

Figure 3. The full band spectra of SSCs 4a (top), 5a (top-middle), 14 (bottom-middle), and 8a (bottom). These spectra are averaged over the FWHM continuum source size and have been corrected for foreground gas (Section 2.4). The continuum has not been removed. There are many lines detected in these clusters, which are marked by the vertical lines and labels (where vib denotes a ro-vibrational transition; see also Krieger et al. 2020). The main lines used in this study (CS 7 − 6 and H^{13}CN 4 − 3) are marked in red (thick solid), lines used to determine the systemic velocity are in orange (thin solid), and other lines are in gray (dashed). The P-Cygni profile is seen in many lines in SSCs 4a, 5a, and 14. In some cases, the absorption is saturated (i.e. absorbed down to zero intensity shown by the horizontal gray lines) especially in the brightest lines (such as CO 3 − 2, HCN 4 − 3, and HCO$^+$ 4 − 3). The CO 3 − 2 line profile is further complicated due to clouds along the line of sight. SSC 8a is shown as an example of bright source without evidence for outflows, though there may be a hint of inflows in CS 7 − 6, H^{13}CN 4 − 3, and HCO$^+$ 4 − 3.

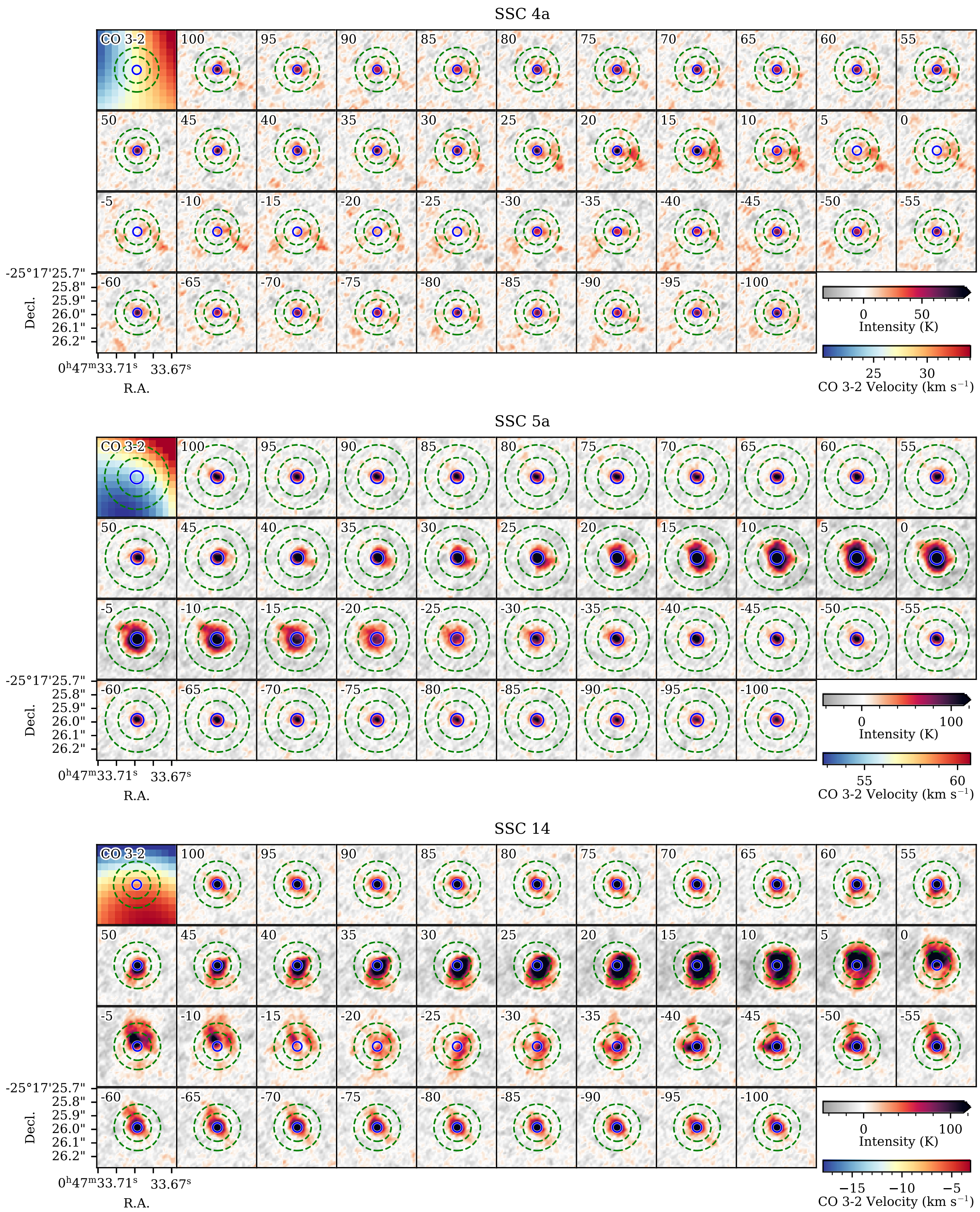

Figure 4. Channel maps around CS 7 − 6 for SSCs 4a (top), 5a (middle), and 14 (bottom) in 10 pc × 10 pc regions. The continuum has not been removed. The first panel shows the smoothed CO 3 − 2 velocity field in this region (Krieger et al. 2019), indicative of the large-scale bulk gas motions. The CO 3 − 2 colorscale and the labeled CS 7 − 6 velocity channels (in km s^{-1}) are relative to the cluster systemic velocity (Table 1). The solid blue circles show the continuum source sizes, and the dashed green annuli show the regions used for the foreground correction. The $H^{13}CN$ 4 − 3 channel maps are similar.

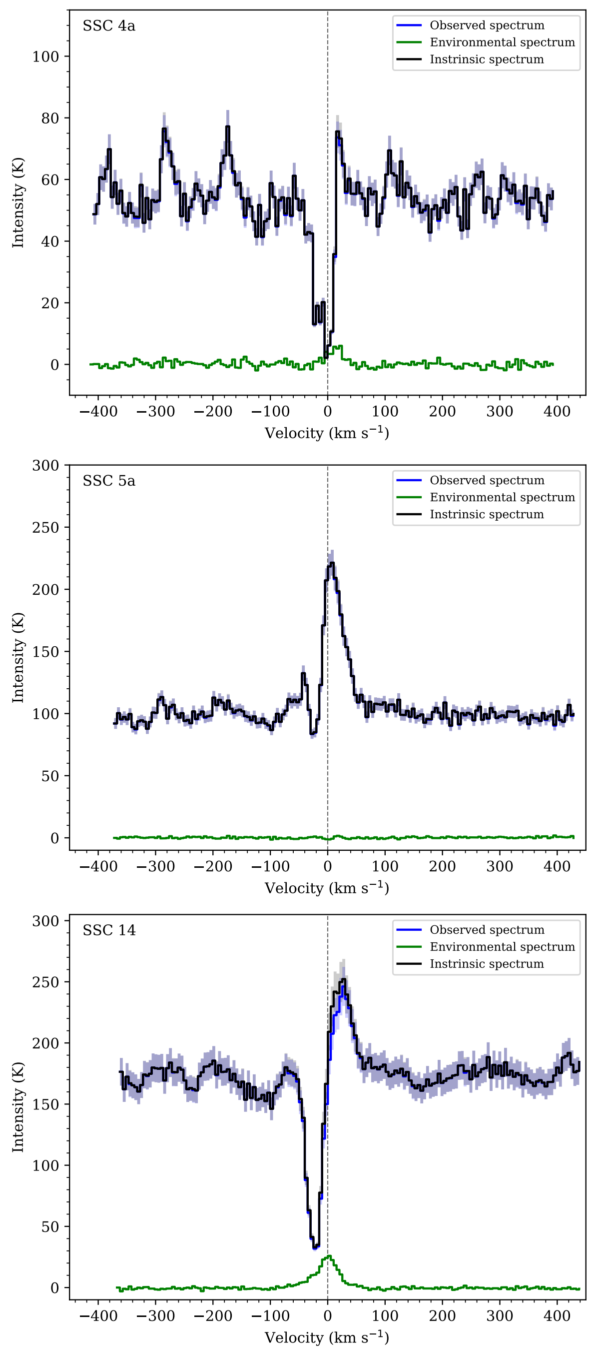

Figure 5. The CS 7 − 6 spectra for SSCs 4a (top), 5a (middle), and 14 (bottom) averaged over the 350 GHz continuum source area (blue; corresponding to the blue ellipses in Figure 4), the foreground gas (green; corresponding to the green annuli in Figure 4), and the corrected, intrinsic CS 7−6 spectrum accounting for the foreground gas (black). The blue shaded region around the observed spectrum reflects the standard deviation of the spectrum within the continuum source area. The gray shaded region around the intrinsic spectrum includes the propagated uncertainties from the assumed excitation temperature ($T_{ex} = 102 \pm 28$ K). See Section 2.4 for details of the foreground gas correction.

over, our method for the foreground correction is quite simplistic, and there are uncertainties related to the fraction of gas that may be associated with the clusters, the geometry of the environmental material, and the assumed excitation temperature. As can be seen in Figure 5, however, the correction mostly affects the peak of the emission components. After the foreground correction, the emission peak for SSC 14 increases by 7% (17 K), whereas the absorption tough only increases by 4.5% (1.5 K). There is no appreciable change in the spectra for SSCs 4a and 5a. The absorption features are, therefore, largely unaffected by this correction, and the derived properties of the outflow (presented in Sections 3.1 and 3.2) are robust.

2.5. *Cluster Systemic Velocities*

We constrain the systemic velocity of all of the detected clusters using the full-band spectra and the detected line list presented by Krieger et al. (2020). Using the full-band spectrum for each cluster, we simultaneously fit each line in the line list using a series of Gaussians of the form

$$I(\nu) = I_{\rm cont} + \sum_{\rm line} I_{\rm line} \exp\left[\frac{-(\nu - \nu_{\rm line-rest})^2}{2\sigma^2_{\rm line}}\right] \qquad (3)$$

where $I_{\rm cont}$ is the fitted continuum level over the whole spectrum, $I_{\rm line}$ is the fitted intensity of each line, $\nu_{\rm line-rest}$ is the fixed rest frequency of each line, $\sigma_{\rm line}$ is the fitted width of each line, and ν is the rest frequency of the observed spectrum which depends on the assumed systemic velocity. The primary lines used to determine the systemic velocity are marked in orange in Figure 3; these lines tend to have strong emission and simple line shapes. Other strong lines in the band (e.g., CO 3 − 2, HCN 4 − 3, HCO^+ 4 − 3) tend to have complicated line shapes that make accurately determining the systemic velocity difficult. Due to the presence of lines with complicated shapes and line-blending, the cross-correlation of each full-band spectrum and the multi-Gaussian fit is done by-eye. The systemic velocities of for all the clusters are listed in Table 1. The uncertainty is estimated to be ±5 km s^{-1}. For SSCs 4a, 5a, and 14, the systemic velocities are further refined and confirmed using other lines in the cleaned CS 7 − 6 and $H^{13}CN$ 4 − 3 cubes (Figure 6). Several of these lines — the vibrational transitions, in particular — have sharp peaks and are spatially localized to the clusters themselves. They, therefore, provide tighter constraints on the cluster systemic velocities. For SSCs 4a, 5a, and 14, we estimate that our cluster systemic velocities are accurate to ±1 km s^{-1}.

2.6. *Outflow Candidates*

We determine our final list of outflow candidates based on robust detections of blueshifted absorption and redshifted emission in the CS 7 − 6 and $H^{13}CN$ 4 − 3 lines. We present SSCs 4a, 5a, and 14 as our conservative list of detected

P-Cygni profiles indicative of outflows. The CS 7 − 6 and $H^{13}CN$ 4 − 3 spectra towards SSCs 4a, 5a, and 14 are shown in Figure 6, which are from the cleaned line cubes (Section 2.2) and have been corrected for foreground gas (Section 2.4).

While other SSCs show absorption features, these are not due to outflowing material as the absorption occurs at the line center. Absorption at the line center is likely due to self-absorption of the cold material surrounding the cluster against the embedded continuum source. Redshifted absorption would be indicative of material inflowing towards the cluster; a hint of inflow is perhaps seen towards SSC 8a (Figure 3, especially the CS 7 − 6, HCN 4 − 3 and HCO^+ 4 − 3 lines). Blueshifted absorption, on the other hand, means that the cold foreground material is outflowing from the cluster. For this analysis, we are focused on the blueshifted absorption indicative of outflows.

We also verify that these absorption features are not induced by the spatial filtering by the interferometer. Due to the incomplete sampling of the Fourier plane and the lack of short spacings, emission on larger scales is filtered out and cannot be properly deconvolved, causing an increase in the RMS of the data at the velocities where bright extended emission would be present. This problem manifests itself as negative "bowls" around bright emission, but also as negative features that have velocity structure. While this mainly affects the continuum (which is not removed from these data), it can also induce false absorption features in the affected velocity range. This can be seen, for example, in the CO 3 − 2 lines in Figure 3, where the absorption profiles are very complex. Our choice to focus on CS 7 − 6 and $H^{13}CN$ 4 − 3 mitigates this problem, as these transitions require high densities to be excited and are hence fairly localized to the clusters themselves, with not much of an extended component. As shown in Figure 5 the environmental CS 7 − 6 spectra around the SSCs are either flat or show the line in emission; the $H^{13}CN$ 4 − 3 spectra show similar profiles. Therefore, we conclude that the CS 7 − 6 and $H^{13}CN$ 4 − 3 absorption features are not a result of the spatial filtering by the interferometer, although it may contribute to uncertainties at the 10% level.

A careful measurement of the cluster systemic velocities (Section 2.5) is critical to determine whether the absorption is blueshifted with respect to the cluster or not. Critically, for a few clusters (e.g., SSCs 3a and 13a) there are pathological combinations of absorption at the line center coupled with strong vibrationally excited lines in emission at the redshifted edge of the absorption feature, which together could masquerade as P-Cygni profiles. We identify other line candidates present in the spectra around CS 7 − 6 and $H^{13}CN$ 4 − 3 using the line list presented by Krieger et al. (2020) as well as Splatalogue[1], which are listed in the shaded yellow regions in Figure 6. It is outside the scope of this paper to verify precisely which other lines are present in the spectra, so we present them simply as possible candidates (or combinations of candidates) which confuse the CS 7 − 6 and $H^{13}CN$ 4 − 3 spectra. This line blending can lead to false detections of P-Cygni profiles. For example, $H^{13}CN$ 4 − 3 $v_2 = 1$ is located 100 MHz ($\approx$ 88 km s^{-1}) red-ward of $H^{13}CN$ 4 − 3, as can be seen in the right column of Figure 6. Similarly, HCN 4 − 3 $v_2 = 1$ is located only 45 MHz ($\approx$ 38 km s^{-1}) red-ward of HCN 4 − 3. Given the broad line profiles (in emission and absorption), these lines can easily blend together to produce a facsimile of a P-Cygni profile. A careful measurement of the cluster systemic velocities (using other lines with simpler profiles), cross-referencing with the line list presented by Krieger et al. (2020), and further verification using Splatalogue[1] reveals that these are not true P-Cygni profiles. It is also worth noting that there is an emission feature (likely $OS^{18}O$, an SO_2 isotopologue) seen in the CS 7 − 6 absorption trough of SSC 4a (upper left panel of Figure 6).

That we detect outflows from SSCs 4a, 5a, and 14 is in large part due to our ability to spatially resolve the individual clusters, since the spectral signatures of the outflows are localized roughly to the central half-flux radius of the clusters. In retrospect, there are indications of these outflows in the CS 7 − 6 and $H^{13}CN$ 4 − 3 line profiles presented by Leroy et al. (2018, see their Figure 3) in SSCs 4 and 14. The much weaker outflow in SSC 5a is not apparent in these lower resolution data where the clusters are only marginally resolved. There are also kinematic offsets between HCN 4−3 and H40α measurements towards these clusters which are consistent with the effects of these outflows at lower resolution (E. A. C. Mills et al., in prep.).

2.7. *Internal Cluster Kinematics*

Briefly here, we investigate whether SSCs 4a, 5a, and 14 exhibit signs of internal rotation. Observational detections of rotation in star and globular clusters in the Milky Way are mixed (e.g. Kamann et al. 2019; Cordoni et al. 2020), though simulations predict that massive star clusters ($>$ 1000 $M_\odot$) should have appreciable rotation (Mapelli 2017).

We investigate the internal kinematics by constructing position-velocity (PV) diagrams over a range of angles as well as peak-velocity and intensity-weighted velocity (moment 1) maps around each of the clusters. While we see no clear signs of internal rotation, the absorption hinders this analysis significantly as it affects the (effective) intensity weighting of the peak- and intensity-weighted velocity (moment 1) maps. It similarly confuses the interpretation of

[1] https://www.cv.nrao.edu/php/splat/advanced.php

the PV diagrams. Therefore, we cannot claim that the SSCs are not rotating, only that, given the presence of absorption, we see no clear evidence for rotation. We also check clusters without absorption or outflow signatures, and also find no evidence of rotation.

3. RESULTS

Using ALMA data at 350 GHz at 1.9 pc resolution, Leroy et al. (2018) identified 14 marginally-resolved clumps of dust emission whose properties are consistent with forming SSCs. In our new 0.5 pc resolution data, many of these SSCs fragment substantially such that there is a bright, massive primary cluster surrounded by smaller satellite clusters (Figure 1). From the 0.5 pc resolution 350 GHz dust continuum image (Figure 1), we identify roughly three dozen clumps of dust emission. We identify candidate outflows towards three SSCs: SSCs 4a, 5a, and 14 (where the appended "a" denotes the primary cluster of the fragmented group). The locations of these clusters within the nucleus of NGC 253 are shown in Figure 1, where the insets show the CS 7−6 line profiles towards these three clusters. In each of these SSCs, we see evidence for blueshifted absorption and redshifted emission in many lines (Figure 3), but we focus on the CS 7−6 and $H^{13}CN$ 4−3 lines (Figure 6) which provide the best balance between bright lines with sufficient SNR, absorption features which do not suffer from saturation effects, and which probe gas localized to the clusters. This line shape is commonly referred to as a P-Cygni profile — for the star in which it was first detected — and is indicative of outflows.

We take two approaches to derive the physical properties of the outflows in each cluster. First, we fit the absorption component of the line profiles to measure the outflow velocity, column density, mass, mass outflow rate, momentum, etc (Section 3.1). Second, we model line profiles of the CS 7−6 and $H^{13}CN$ 4−3 spectra towards each cluster with the goal of constraining the outflow opening angles and orientations to the line of sight (Section 3.2). While the primary goal of the line profile modeling is to constrain the outflow geometry, it also provides a measurement of the outflow velocity, column density, mass, mass outflow rate, etc. We compare common parameters of these methods in Section 3.3.

3.1. *Outflow Properties from Absorption Line Fits*

For a first estimate, we measure the outflow velocities, column densities, gas masses, and momentum of each outflow by fitting the profiles of $H^{13}CN$ 4−3 and CS 7−6 with a two-component Gaussian (blue dashed curves in Figure 6). We exclude the portions of the spectra that may be contaminated by other lines, as marked by the yellow shaded regions in Figure 6. The fit to the absorption feature yields the velocity at the maximum absorption ($V_{max-abs}$), or the velocity at which the bulk of the material is outflowing. We define the maximum outflow velocity as 2σ from the average velocity ($V_{max,out} \equiv V_{max-abs} + 2\frac{\Delta V_{out,FWHM}}{2.355}$), which means that 95% of the material traced by CS 7−6 and $H^{13}CN$ 4−3 has an outflow velocity slower than $V_{max,out}$ (for a truly Gaussian line). Given the mean outflow velocity and the cluster size, we calculate the crossing time, or the time for a parcel of gas to travel from the center of the cluster to the edge ($t_{cross} \equiv r_{SSC}/V_{max-abs}$), where r_{SSC} is equivalent to the half-flux radius (Table 1). From the fitted absorption to continuum intensity ratio, we derive the optical depth and hence the column density in absorption. We convert from the column density of the molecule to H_2 ($N_{H_2,out}$) using abundances from Martín et al. (2006). From the column density and projected size (Table 1), we estimate the H_2 mass in the outflow ($M_{H_2,out}$) assuming the outflow is spherical. Constraints on the opening angle of the outflows derived from modeling of the line profiles are discussed in Section 3.2 and show that the outflows must be nearly spherical. Given the mass, crossing time, and mean outflow velocity, we calculate the mass outflow rate ($\dot{M}_{H_2,out}$), the gas removal timescale ($t_{remove-gas}$), the radial momentum injected per unit stellar mass in the cluster (p_r/M_*), and the kinetic energy of the outflow (E_{kin}). Further details and equations used to derive these quantities are presented in Appendix A. The outflow parameters derived from the absorption profile fits are reported in Table 2.

The clusters have outflows with maximum velocities ($V_{max,out}$) of $\sim 40-50$ km s^{-1}. For all three SSCs with outflows, $V_{max,out}$ is larger than the escape velocity (V_{escape}; reproduced in Table 2 from Leroy et al. 2018). The bulk of the material traced by CS 7−6 and $H^{13}CN$ 4−3, however, has velocities less than V_{escape} (as traced by $V_{max-abs}$). For SSCs 4a, 5a, and 14, 20%, 7%, and 7% of the outflowing material has velocities larger than the escape velocity and will be able to escape from the cluster. The gas crossing time (t_{cross}) is $\sim$few$\times 10^4$ years, which is a lower limit on the age of the outflow as discussed further in Section 4.1.

The masses in the outflows are large. The molecular hydrogen column densities and masses derived from $H^{13}CN$ 4−3 are larger than those derived from CS 7−6 in all cases. One possibility is that CS 7−6 is more optically thick than $H^{13}CN$ 4−3, which may be supported by the depth of the absorption in SSC 4a, but this cannot explain the discrepancy in SSC 5a. A more likely possibility is that the relative molecular abundances we assume are not correct for these small, extreme regions. We adopt molecular abundances for $H^{13}CN$ and CS with respect to H_2 of $[H^{13}CN]/[H_2] = (1.2 \pm 0.2) \times 10^{-10}$ and $[CS]/[H_2] = (5.0 \pm 0.6) \times 10^{-9}$ from a study of the the center of NGC 253 at 14–19″ ($\sim 240-320$ pc) resolution by Martín et al. (2006). Adopting these abundances on the parsec scales of our clusters, however, is highly uncertain. Observations of envelopes around high-mass young stellar objects in the Milky Way, for example, reveal order-of-magnitude variations in the abundances of molecules, especially nitrogen and

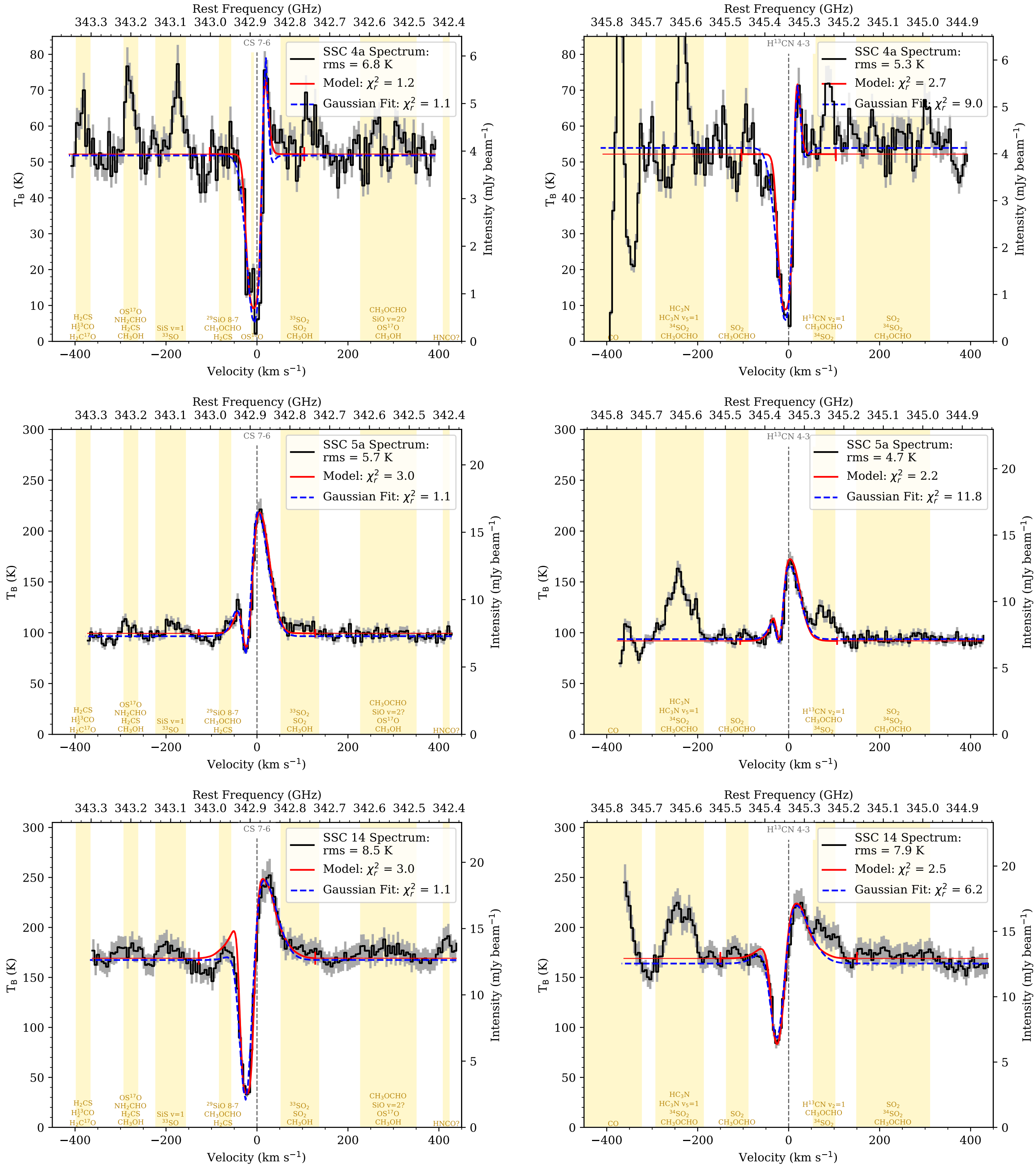

Figure 6. The CS 7 – 6 (left) and $H^{13}CN$ 4 – 3 (right) spectra for SSCs 4a (top), 5a (middle), and 14 (bottom). The yellow shaded regions show where other lines may contaminate the spectrum. Possible candidate lines are listed at the bottom of the yellow shaded regions. The dashed blue curves show the two-component Gaussian fit to the profile (Section 3.1). The solid red curves show the best-fitting spherical outflow models (Section 3.2). The vertical red line segments shows the range of velocities actually modeled, the red curve outside of these vertical line segments is an extrapolation.

Table 2. Cluster and Outflow Properties from Absorption Line Fits

Quantity	Unit	SSC 4a		SSC 5		SSC 14	
		CS 7−6	$H^{13}CN$ 4−3	CS 7−6	$H^{13}CN$ 4−3	CS 7−6	$H^{13}CN$ 4−3
$\log_{10}(M_{H_2,tot})$ [a]	$\log_{10}(M_\odot)$	5.1		5.3		5.7	
$\log_{10}(M_*)$ [b]	$\log_{10}(M_\odot)$	5.0		5.4		5.5	
V_{escape} [c]	km s^{-1}	22.0		33.2		45.5	
τ [d]		2.3	2.3	0.2	0.0	1.8	0.6
$V_{max-abs}$ [e]	km s^{-1}	6	6	22	20	24	24
$V_{out,max}$ [f]	km s^{-1}	40	46	42	34	51	56
$\Delta V_{out,FWHM}$ [g]	km s^{-1}	40	46	24	17	32	38
$\log_{10}(t_{cross})$ [h]	$\log_{10}$(yr)	5.0	5.0	4.5	4.6	4.4	4.4
$\log_{10}(N_{H_2,out})$ [i]	$\log_{10}(cm^{-2})$	23.9	25.3	22.7	23.2	23.7	24.6
$\log_{10}(M_{H_2,out})$ [j]	$\log_{10}(M_\odot)$	4.7	6.1	3.8	4.3	4.6	5.5
$\log_{10}(M_{H_2,out}/M_{H_2,tot})$ [k]		-0.4	1.0	-1.5	-1.0	-1.1	-0.2
$\log_{10}(M_{H_2,out}/M_*)$ [k]		-0.3	1.1	-1.6	-1.1	-0.9	-0.0
$\log_{10}(\dot{M}_{H_2,out})$ [l]	$\log_{10}(M_\odot\ yr^{-1})$	-0.3	1.1	-0.7	-0.3	0.2	1.1
$\log_{10}(t_{remove-gas})$ [m]	$\log_{10}$(yr)	5.4	4.0	6.0	5.6	5.5	4.6
$\log_{10}(p_r/M_*)$ [n]	$\log_{10}(km\ s^{-1})$	0.7	2.1	0.0	0.5	0.7	1.6
$\log_{10}(E_{kin})$ [o]	$\log_{10}$(erg)	49.2	50.6	49.6	49.9	50.4	51.3

NOTE—Values (aside from the top three) are derived from fits to the absorption component of the line profiles. See Section 3.1 and Appendix A for details on how these values were calculated.

[a] The cluster gas mass measured from the dust continuum and assuming a gas-to-dust ratio of 100 (Leroy et al. 2018). Uncertainties are ∼0.4–0.5 dex, with these measurements likely biased low due to assumptions about the dust temperature, dust-to-gas ratio, and the dust opacity.

[b] The cluster zero age main sequence (ZAMS) stellar mass measured from the 36 GHz free-free emission (Leroy et al. 2018). Systematic uncertainties are ±20%. Larger uncertainties are dominated by the unknown amount of ionizing photons absorbed by dust and the possibility of the clusters being evolved beyond the ZAMS. Both of these effects mean that the stellar masses are biased low. However, the stellar masses for these clusters derived at lower resolution from radio recombination lines (E. A. C. Mills et al., in prep.) are at most 0.2 dex larger than these values.

[c] The escape velocity from the cluster (Leroy et al. 2018). Uncertainties are dominated by those from the gas and stellar masses.

[d] The optical depth in the outflow calculated from the absorption to continuum ratio (Eq. A4).

[e] The velocity where the absorption is maximized, corresponding to the velocity at which the bulk of the material traced by CS 7−6 and $H^{13}CN$ 4−3 is outflowing.

[f] The maximum outflow velocity, defined as 2σ from the mean outflow velocity (Eq. A3). For a Gaussian line, this means that 95% of the dense material has an outflow velocity slower than $V_{max,out}$.

[g] The FWHM line width from the Gaussian fit to the absorption feature.

[h] The gas crossing time, or the time it would take a parcel of gas to travel from the center of the cluster to r_{SSC} at $V_{max-abs}$ (Eq. A2).

[i] The H_2 column density in the outflow derived from τ (Eqs. A5–A9). This calculation assumes LTE with an excitation temperature of 130 ± 56 K and abundances of CS 7−6 and $H^{13}CN$ 4−3 relative to H_2 from Martín et al. (2006). The abundances may vary by an order-of-magnitude on these small scales, so all quantities which depend on the column density are limited to order-of-magnitude precision. The blueshifted outflow component only probes the portion of the outflow on the approching side, so the values are multiplied by 2 to account for the receding side of the outflow, assuming it is identical to the approaching side. Uncertainties are ±1 dex.

[j] The H_2 mass in the outflow derived from $N_{H_2,out}$ and the projected cluster size (Eq. A10). This calculation and others which depend on it assume the outflow is spherical, which is supported by the results of our modeling (Section 3.2). Uncertainties are ±1 dex.

[k] The H_2 mass in the outflow compared to the total gas or stellar mass in the cluster. Uncertainties are ±1 dex.

[l] The mass outflow rate derived over one crossing time (Eq. A11). Uncertainties are ±1 dex.

[m] The gas removal time, or the time it would take for the current mass outflow rate to expel all of the cluster gas mass ($M_{H_2,tot}$) from the clusters (Eq. A12). Uncertainties are ±1 dex.

[n] The radial momentum carried by the outflow per unit stellar mass, which also assumes the outflow is spherical (Eq. A13). Uncertainties are ±1 dex.

[o] The kinetic energy of the outflow calculated from $M_{H_2,out}$ and $V_{max-abs}$ (Eq. A14). Uncertainties are ±1 dex.

sulfur bearing species (van Dishoeck & Blake 1998, and references therein). The impact of the uncertainty on the fractional molecular abundances is that they translate into order-of-magnitude accuracy for the H_2 column density measurements, as well as the subsequent calculations which depend on the column density, as reported in Table 2. In the following subsection we discuss in more detail what we know about chemical abundances and their variation: our conclusion is that the masses derived from $H^{13}CN$ $4-3$ are likely more accurate.

3.1.1. *Fractional Abundance Variations*

To explain the discrepancies between our abundance-dependent measurements ($N_{H_2,out}$, $M_{H_2,out}$, $\dot{M}_{H_2,out}$, and $t_{remove-gas}$) from CS $7-6$ and $H^{13}CN$ $4-3$ would require that either [CS]/[H_2] is enhanced and/or [$H^{13}CN$]/[H_2] is reduced in these clusters compared to the values measured by Martín et al. (2006), where the brackets refer to the abundance of that species. In the case of CS, modeling by Charnley (1997) shows that [CS]/[H_2] varies from $\sim 10^{-10}-10^{-8}$ depending on age, O_2 abundance, and temperature, with CS being most abundant after $\sim 10^4$ years, at low O_2 abundance, and at low temperatures (T$\sim$100 K) though the trend with temperature is not monotonic. Estimates of the kinetic temperatures of the (marginally resolved) clusters vary from $\sim 200-300$ K (Rico-Villas et al. 2020). At $\sim 10^5$ years (the ZAMS ages of these clusters; Rico-Villas et al. 2020) and a temperature of 300 K, Charnley (1997) find [CS]/[H_2] $\sim 4\times10^{-9}$ depending on the assumed temperature and O_2 abundance, very close to our assumed ratio of $(5.0\pm0.6)\times10^{-9}$ measured by Martín et al. (2006). From CS, SO, and SO_2 line ratios towards these clusters, Krieger et al. (2020) suggest that [CS]/[H_2] may be enhanced by a factor of 2–3 from the values measured by Martín et al. (2006). For SSCs 5a and 14, an enhancement of [CS]/[H_2] by a factor of 2–3 brings our abundance-dependent measurements into much better agreement with those derived from $H^{13}CN$ $4-3$, but this is not sufficient for SSC 4a. The gas in SSC 4a is likely more optically thick than in SSCs 5a and 14, as seen in the absorption to lower temperatures (~ 7 K), which could help explain the lingering discrepancy in this cluster.

In the case of [$H^{13}CN$]/[H_2], Colzi et al. (2018) find that chemical evolution does not affect nitrogen fractionation, so the main driver of a different [$H^{13}CN$]/[H_2] in these SSCs would be due to changes in the $^{12}C/^{13}C$ ratio. If there is less ^{13}C in these clusters compared to the environment, then [$H^{13}CN$]/[H_2] may be lower. Towards these clusters, Krieger et al. (2020) find hints that $^{12}C/^{13}C$ may be on the high side of the assumed ratio of 40 ± 20 (Martín et al. 2010, 2019; Henkel et al. 2014; Tang et al. 2019). If the the ^{12}C abundance remains the same, this suggests that reductions in ^{13}C and hence [$H^{13}CN$]/[H_2] are possible. To bring our abundance-dependent measurements from $H^{13}CN$ $4-3$ into agreement with the lower values derived from CS $7-6$ would imply $^{12}C/^{13}C \gtrsim 300$, much larger than even the highest ratios measured in NGC 253 (Martín et al. 2010) while keeping ^{12}C fixed. Changing [$H^{13}CN$]/[H_2], therefore, likely plays a minor role in remedying the differences in our abundance-dependant quantities.

If, therefore, the discrepancy between our abundance-dependent quantities measured from CS $7-6$ and $H^{13}CN$ $4-3$ is due to a change in the abundances of those species, the effect is likely driven by CS which is enhanced relative to our assumed [CS]/[H_2] with perhaps a small contribution from reduced [$H^{13}CN$]/[H_2]. As a result, the abundance-dependant quantities derived from $H^{13}CN$ $4-3$ are likely more accurate. In the values presented here and in the following section, we adopt the abundances measured by Martín et al. (2006) and maintain the conservative order-of-magnitude uncertainties on these quantities.

3.2. *Outflow Properties from Line Profile Modeling*

The short gas crossing times, large outflow masses, and outflow mass rates (Table 2) suggest the outflow activity in these objects cannot be sustained for a long time. From this standpoint, it is reasonable that we detect outflows in $\lesssim$10% of the SSCs, so it is possible that we are indeed catching a small fraction of the SSCs in this short-lived phase. The analysis in Section 3.1, however, implicitly assumes that the outflows are spherical. Another possibility, however, is that the outflows are biconical with a more-or-less narrow opening angle. In that case the outflows from the three clusters we identify are serendipitously pointed close enough to the line of sight to make them detectable. If the observed outflows are not spherical, geometric correction factors will need to be applied to the measured quantities in Table 2, and more outflows could exist that we do not detect because their geometry is unfavorable.

In order to determine whether the observed outflows are spherical or biconical and how they are oriented with respect to the line of sight, we build a simple radiative transfer model to model the spectrum through the outflow. We consider spherical and biconical outflows, where the opening angle (θ) and orientation to the line of sight (Ψ) of the biconical outflows can be varied. Opening angles are defined as the full-angle for one hemisphere; the maximum opening angle is $\theta = 180°$, corresponding to a sphere. Technical details and equations are presented in Appendix B, but we summarize the basic scheme here. We construct a four-dimensional box (x, y, z, ν), where radii are measured in spherical coordinates from the center of the box. We define the measured cluster radius such that $r_{SSC} = r_{half-flux}$ (Table 1). The simulated box is scaled to $4\times r_{SSC}$ in each spatial dimension (x, y, z) to fully encompass the line emission (e.g. Figure 4) especially since

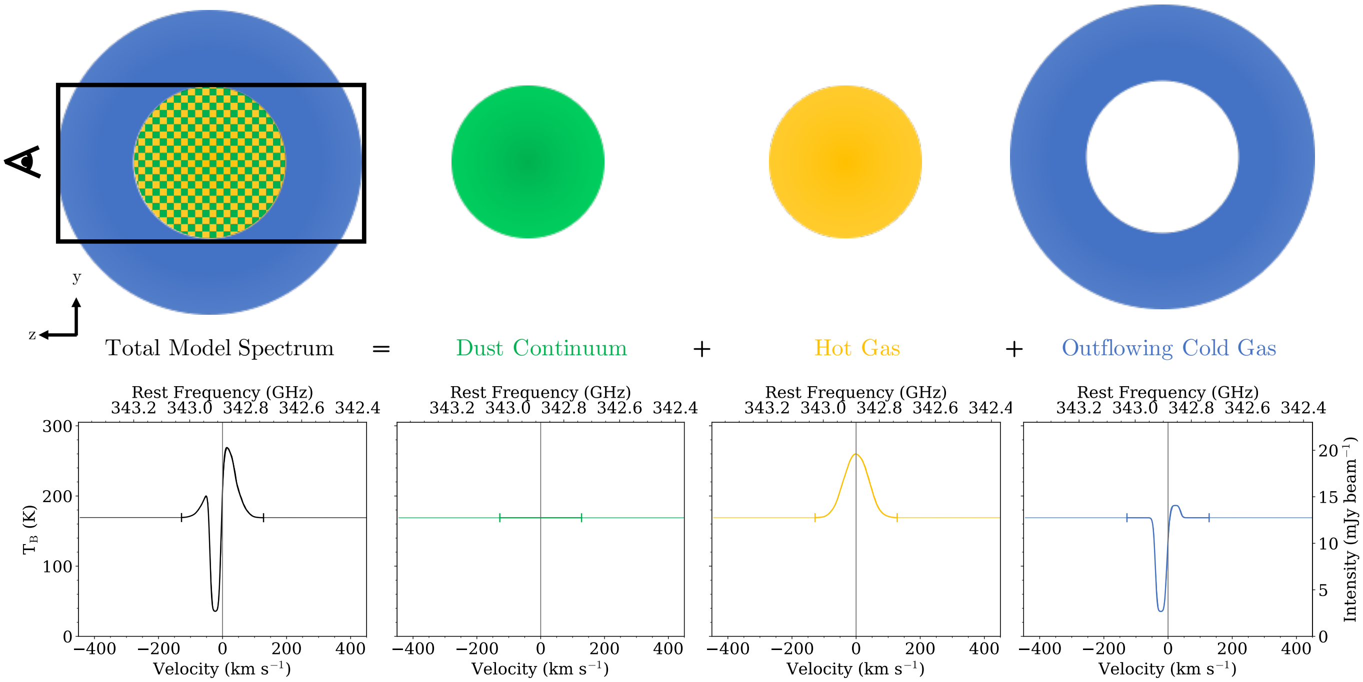

Figure 7. A 2D schematic showing the three physical components of the model at a slice through the box at $x = 0$ and their spectral contributions. The black rectangle shows the slice of the field of view used to calculate the final spectrum. A representative spectrum for each component is shown below the corresponding 2D schematic. CS 7 – 6 towards SSC 14 is used here as an example. The thicker curves bounded by the vertical line segments show the velocity range modeled, whereas the thin curves outside are an extrapolation. The hot gas and cold outflowing gas spectra include the dust continuum component so that the absorption due to the outflowing components is visible.

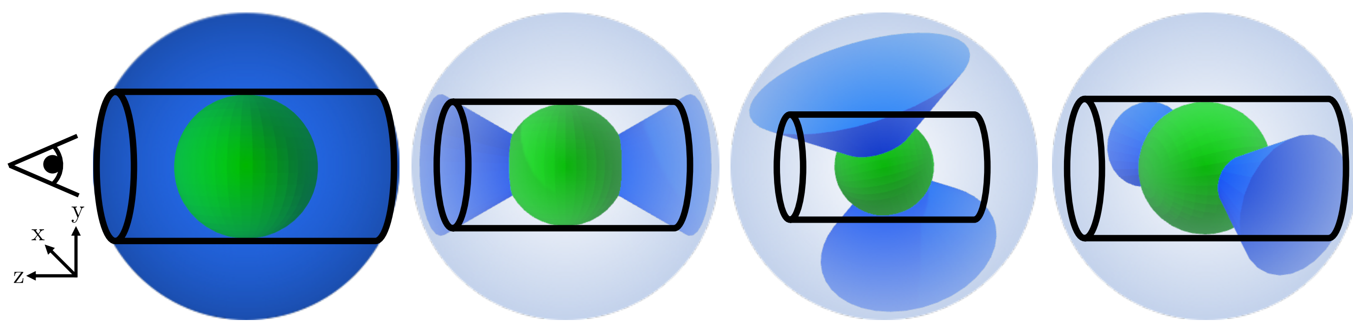

Figure 8. 3D schematics of (from left to right) a spherical ($\theta = 180^\circ$) outflow, a biconical ($\theta = 60^\circ$) outflow pointed along the line of sight, and biconical ($\theta = 90^\circ$ and $\theta = 45^\circ$) outflows that are inclined to the line of sight ($\Psi = 95^\circ$ and $\Psi = 60^\circ$). The green central sphere includes both the dust continuum and hot gas components and has $r = r_{SSC}$. The dark blue outer shell or cones show the outflowing gas. The light blue component shows the ambient gas between the outflow cones. The black cylinder shows the line of sight and field of view over which the model spectrum is integrated and averaged, which has $r = r_{SSC}$ (in the xy-plane) and spans $4 \times r_{SSC}$ along the z-axis.

the geometry along the line of sight (z-axis) is unknown. The velocity axis is scaled based on the input outflow velocity and velocity dispersion, so that the velocity resolution is optimized over the velocities relevant for the cluster and outflow; this is described more fully in Appendix B. Three physical components are required to adequately model the CS 7 – 6 and $H^{13}CN$ 4 – 3 spectra, as shown in Figures 7 and 8. These components and the input parameters for each are described below. The input parameters are denoted with * in Table 3, which lists input parameter values that yield the best model fits. Radial profiles of these components and the input parameters are summarized in Figure B2 in Appendix B.

1. Dust continuum component: Shown in green in Figures 7 and 8, this component is a sphere with $r = r_{SSC}$ and a constant (in space and frequency) temperature (T_{cont}). The optical depth in a single cell is a maximum ($\tau_{cont,max}$) at the center, then decreases like a Gaussian with FWHM $= 2 \times r_{SSC}$. In other words, the FWHM of the dust continuum optical depth profile matches the

Table 3. Line Profile Modeling Input Parameters and Calculated Values

		SSC 4a		SSC 5		SSC 14	
Quantity	Unit	CS 7−6	$H^{13}CN$ 4−3	CS 7−6	$H^{13}CN$ 4−3	CS 7−6	$H^{13}CN$ 4−3
$V_{max-abs}$ [*,a]	km s^{-1}	7	7	25	22	25	28
$\Delta V_{out,FWHM}$ [*,b]	km s^{-1}	25	25	20	15	20	25
$V_{out,max}$ [c]	km s^{-1}	28	28	42	35	42	49
$\log_{10}(t_{cross})$ [d]	$\log_{10}$(yr)	4.9	4.9	4.5	4.6	4.4	4.3
$\Delta V_{hot,FWHM}$ [*,b]	km s^{-1}	10	10	50	50	80	85
T_{out} [*,e]	K	7	7	25	20	35	40
T_{hot} [*,f]	K	900	900	800	800	800	800
T_{cont} [*,g]	K	105	105	200	185	340	340
$\log_{10}(n_{out})$ [*,h]	$\log_{10}(cm^{-3})$	7.8	7.5	5.5	5.9	6.2	6.8
$\log_{10}(n_{hot})$ [*,h]	$\log_{10}(cm^{-3})$	8.6	9.9	8.8	9.8	8.8	10.0
$\log_{10}(\tau_{cont,max})$ [*,i]		-1.3	-1.3	-1.3	-1.3	-1.3	-1.3
$\log_{10}(N_{H_2,out})$ [j]	$\log_{10}(cm^{-2})$	25.4	25.1	23.2	23.7	24.0	24.5
$\log_{10}(M_{H_2,out})$ [j]	$\log_{10}(M_\odot)$	6.3	6.0	4.4	4.9	5.3	5.4
$\log_{10}(\dot{M}_{H_2,out})$ [j]	$\log_{10}(M_\odot\ yr^{-1})$	1.4	1.1	-0.1	0.3	0.9	1.1
$\log_{10}(t_{remove-gas})$ [j]	$\log_{10}$(yr)	3.7	4.0	5.4	5.0	4.8	4.6

NOTE—The input and output or derived parameters for the best-fitting spherical outflow models. See Section 3.2 and Appendix B for details.

[*] Best-fit input parameters to the model. The uncertainties listed below are reflective of the grid of tested parameters.

[a] The outflow velocity, which is assumed constant. Uncertainties are ±1 km s^{-1}.

[b] The FWHM velocity dispersion of the given component. Uncertainties are ±2 km s^{-1}.

[c] The maximum outflow velocity defined as $V_{max-abs} + 2\frac{\Delta V_{out,FWHM}}{2.355}$. Propagated uncertainties are ±2 km s^{-1}.

[d] The gas crossing time defined as $\frac{r_{SSC}}{V_{max-abs}}$. Propagated uncertainties are 4% for SSCs 14 and 5 and 14% for SSC 4a.

[e] The gas temperature in the outflow at the line peak, which is constant spatially. Uncertainties are ±2 K.

[f] The gas temperature in the hot component at the line peak, which is constant spatially. Uncertainties are ±25 K.

[g] The continuum temperature, which is constant spatially and spectrally. Uncertainties are ±5 K.

[h] The log of the peak H_2 number density for the given component. Uncertainties are ±0.25 dex.

[i] The peak optical depth of the continuum component. Uncertainties are ±0.025.

[j] Uncertainties are ±1 dex due to the molecular abundance ratios relative to H_2.

diameter of the 350 GHz continuum source. The temperature and optical depth are set to zero for $r > r_{SSC}$.

2. Hot gas: Shown in yellow in Figure 7 (and encompassed within the green sphere in Figure 8), this spherical component is required to reproduce the strong emission component of the P-Cygni profiles. This component is defined by an input hot gas temperature (T_{hot}), a H_2 volume density (n_{hot}) for the central ($r = 0$) pixel, and a velocity dispersion ($\Delta V_{hot,FWHM}$). T_{hot} is constant (spatially) for $r \leq r_{SSC}$, and is set to zero outside. The density falls off $\propto r^{-2}$ from the center and is set to zero for $r > r_{SSC}$. The line is centered on zero velocity along the frequency axis, and the Gaussian linewidth is given by $\Delta V_{hot,FWHM}$. Using the equations in Appendix B, this produces a spectrum at every pixel in the box.

3. Cold, outflowing gas: Shown in blue in Figures 7 and 8, this is the outflow component which produces the absorption features. This component is defined by an input gas temperature (T_{out}), a H_2 volume density (n_{out}) at the cluster boundary ($r = r_{SSC}$), a constant outflow velocity (V_{out}), a velocity dispersion ($\Delta V_{out,FWHM}$), an opening angle (θ), and an orientation to the line of sight (Ψ). The gas temperature is constant (spatially) within this component. The density is a maximum at $r = r_{SSC}$ and deceases $\propto r^{-2}$ until the edges of the box; the density is set to zero inside the cluster ($r < r_{SSC}$). In the spectral dimension, the line has a centroid velocity given by V_{out} and a FWHM linewidth of $\Delta V_{out,FWHM}$. Using the equations in Appendix B, this produces a spectrum at every pixel in the box. Since the outflow velocity is constant and the density $\propto r^{-2}$, the outflow conserves mass, energy, and momentum. To create a

biconical outflow with the input opening angle (θ), the velocity of the pixels outside the outflow cones is set to zero. This creates an ambient gas component (shown in light blue in Figure 8), which has the same temperature, density, and velocity dispersion properties as the outflowing gas (but with $V_{out} = 0$). The box is then rotated to the input orientation from the line of sight (Ψ).

Together, these three components are integrated from the back of the box forward (e.g. along the $-z$-axis in Figures 7 and 8). To obtain the final spectrum, only pixels within a cylinder along the line of sight with $r = r_{SSC}$ are integrated (shown as the black cylinder in Figure 8) to best compare with the measured spectra which are extracted only over an area corresponding to the continuum source half-flux radius. We adjust the input parameters component-by-component to find the model spectrum that best matches the observed CS $7-6$ and $H^{13}CN$ $4-3$ spectra for SSCs 4a, 5a, and 14. There are degeneracies among input parameters, which are described below and in Appendix B. These best-fit models are shown in red in Figure 6, and the best-fit parameters for CS $7-6$ and $H^{13}CN$ $4-3$ are listed in Table 3. For all spectra and sources, the spherical model provides the best fit, implying that the opening angles of the outflows need to be broad to explain the observed line profiles. A wide opening angle is in agreement with recent magneto-hydrodynamic (MHD) simulations, which show that cluster outflows are asymmetric and chaotic, but still wide-angle in general and regardless of the precise feedback mechanism (e.g., Skinner & Ostriker 2015; Kim et al. 2018; He et al. 2019; Geen et al. 2020a, L. Lancaster et al. in prep.). From these best fit models, we also calculate the H_2 column density and mass in the outflows, which are also listed in Table 3.

We tested models with a fourth physical component representing a fast outflowing component. This was mainly motivated by SSC 14 and the mismatch between the spectrum and model at the blue-ward edge of the absorption feature for both CS $7-6$ and $H^{13}CN$ $4-3$ (Figure 6). In the model, this component is otherwise identical to the "slow" outflow component described above but with a larger outflow velocity and velocity dispersion and a different maximum H_2 volume. While including this component did marginally improve the fits — especially for SSC 14 — the improvement was not enough to justify the additional three parameters introduced into the model.

Our model assumes a constant outflow velocity and r^{-2} density profile to conserve mass, energy, and momentum in the outflow. In reality, a constant outflow velocity is unlikely to be precisely the case, due to turbulence within the outflow itself (e.g., Raskutti et al. 2017) and because the outflow may decelerate as it encounters the surrounding medium. From the data, we investigate the location of the absorption trough

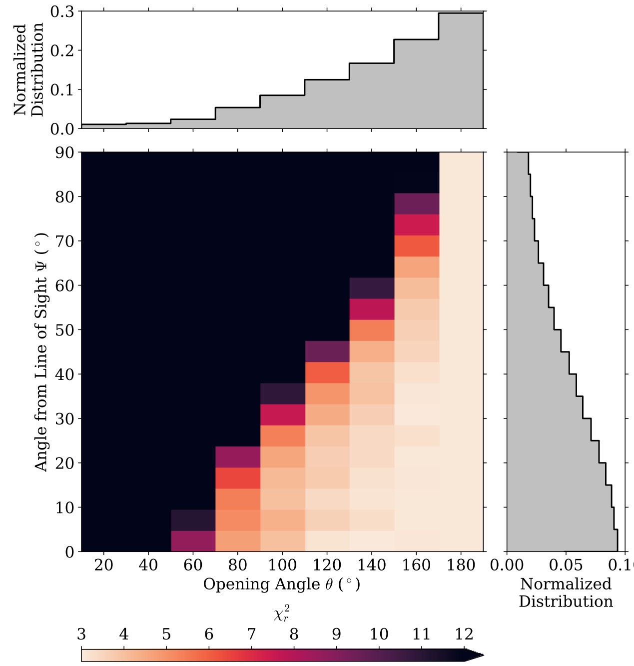

Figure 9. A heatmap showing the reduced chi-squared (χ_r^2) values for models with varying opening angles (θ) and orientations from the line of sight (Ψ) for the same input parameters as listed in Table 3 for CS $7-6$ in SSC 14. The gray histograms show the marginalized distributions for θ (top) and Ψ (right), normalized to unit area. This shows that the outflow opening angles must be wide and/or closely aligned with the line of sight.

around and across the sources. We see no strong evidence for systematic velocity shifts around or across SSCs 4a, 5a, or 14.

There are ranges of opening angles (θ) and orientations (Ψ) which are degenerate and will produce similar output spectra. To investigate how well we can constrain θ and Ψ, we run a grid of models with the same input parameters as in Table 2 with varying θ in steps of 20° and Ψ in steps of 5°. The results for CS $7-6$ in SSC 14 are displayed in Figure 9, which shows that wide outflows and/or those pointed close to the line of sight are strongly favored. Wide angle outflows from clusters are in agreement with results of numerical simulations as mentioned previously. Though the outflows in simulations are clumpy and highly non-uniform, they cover nearly 4π steradians and hence approach the spherical limit of our simple modeling. Narrow and/or off-axis opening angles substantially increase the required input density in out models and result in unphysical solutions for the outflowing mass. In any case, we cannot pin down the precise opening angle and/or line of sight orientation from this modeling, but we place limits on them that suggest the dearth of clusters with observed outflows is not a selection bias due to geometrical effects. It is possible that we miss outflows if the dense gas is very optically thick and therefore obscures underlying outflow signatures (e.g., Aalto et al. 2019). We could also miss weak outflows below our detection limit of sensitivity and cluster mass.

3.3. *Comparing the Two Methods*

The two methods of measuring the outflow properties described have calculated quantities in common. In Figure 10, we compare the velocity where the absorption is maximum ($V_{max-abs}$), the FWHM of the absorption feature ($\Delta V_{out,FWHM}$), the maximum outflow velocity ($V_{out,max}$), the gas crossing time (t_{cross}), the H_2 column density in the outflow ($N_{H_2,out}$), the H_2 mass in the outflow ($M_{H_2,out}$), the mass outflow rate ($\dot{M}_{H_2,out}$), and the time to remove all of the gas mass of the cluster at the current $\dot{M}_{H_2,out}$ ($t_{remove-gas}$). The equations used to calculate these parameters are given in Appendices A and B for the absorption line fits and line profile modeling respectively. The vertical axis of Figure 10 shows the logarithm of the ratio of the quantities derived from each method; each major tick mark and horizontal gridline corresponds to an order of magnitude difference. In general, there is good agreement between the two methods for the quantities which depend on the velocity of the outflow ($V_{max-abs}$, $\Delta V_{out,FWHM}$, ($V_{out,max}$), and t_{cross}). The uncertainties in Figure 10 reflect the order-of-magnitude adopted uncertainties around the abundance ratios, as discussed in Section 3.1.

Given the uncertainties the agreement between the absorption line fits and the line profile modeling is good, especially for $H^{13}CN$ 4 − 3. A notable exception is for CS 7 − 6 in SSC 4a, where the line profile modeling yields 1.5 dex larger H_2 columns and masses than derived from the absorption line fits. This is likely because the CS 7 − 6 absorption in SSC 4a is the most saturated (i.e., the closest to zero). For the absorption line fits, this renders a more uncertain optical depth (from the absorption to continuum ratio) as small changes in the absorption depth leads to large changes in the optical depth and hence the column density. For the line profile modeling, the depth of the absorption depends on the assumed gas temperature and H_2 volume density in the outflow. The bottom of the absorption trough sets an upper limit on the assumed gas temperature in the outflow (T_{out}); in the modeling, the temperature of the absorption tough cannot be lower than the assumed T_{out}. In the case of SSC 4a, this temperature is low ($\sim$ 7 K), well below the temperature needed to excite the $J = 7$ level of CS of 66 K (Schöier et al. 2005)[2]. As a result, the H_2 density in the outflow must be increased, leading to a large outflowing mass. We assume a constant temperature in the outflowing gas, whereas a temperature gradient is likely needed to produce this absorption depth. Because the other sources and lines have shallower absorption depths, they do not suffer from this effect. Other strong lines—HCN 4 − 3 and HCO^+ 4 − 3—shown in Figure 3 also suffer from this saturation, which is why they are not the focus of this analysis. We, therefore, suggest that the column density, mass, and mass outflow rate from the modeling are overestimated in the case of CS 7 − 6 in SSC 4a. This effect is not seen in the absorption line fitting because the absorption to continuum ratio is used to infer the optical depth, but an excitation temperature of 130 K is assumed to derive the level populations (Appendix A). In the line profile modeling, the input gas temperature (7 K in the case of CS 7 − 6 in SSC 4a) is used to derive the level populations instead (Appendix B). Discrepancies between the two methods are also seen in both lines towards SSC 5a, though they are not as extreme as for SSC 4a. The discrepancies in SSC 5a cannot, however, be explained by saturation. The same abundance ratios are used for both methods and these enter into the calculations in the same way, so this discrepancy cannot be remedied by changing [CS]/[H_2].

3.4. *Recommended Values*

Given the number of assumptions of the line profile modeling and the parameter covariances, we suggest that the outflow properties from the absorption line fits presented in Table 2 are more reliable and should be adopted. The assumption of spherical outflows in computing those numbers is substantiated by the modeling, which strongly favors wide outflows (Figure 9). It is encouraging that the line profile modeling generally finds similar values for the outflowing mass, but there are cases where the model likely overestimates the outflowing mass (e.g., SSC 4a). Both sets of measurements are limited in the same way by the uncertainty on the molecular abundances with respect the H_2. As discussed in Section 3.1.1, discrepancies between quantities derived from CS 7 − 6 and $H^{13}CN$ 4 − 3 may be driven primarily by changes in [CS]/[H_2] relative to the assumed abundance, so that quantities derived from $H^{13}CN$ 4 − 3 may be more reliable. Studies, such as the ALMA Comprehensive High-Resolution Extragalactic Molecular Inventory (ALCHEMI)[3], that measure abundances at higher spatial resolution than currently available in these extreme environments may improve the accuracy of our column density, mass, mass outflow rate, and gas removal timescale estimates.

4. DISCUSSION

The existence of outflows in SSCs 4a, 5a, and 14 suggests these clusters may be in a different evolutionary stage compared to the other SSCs in the starburst. In the following section, we investigate the relationship between various timescales relevant to the clusters (4.1) and possible outflow

[2] This information was retrieved from the Leiden Atomic and Molecular Database (LAMDA) on 2020-10-30.

[3] https://alchemi.nrao.edu

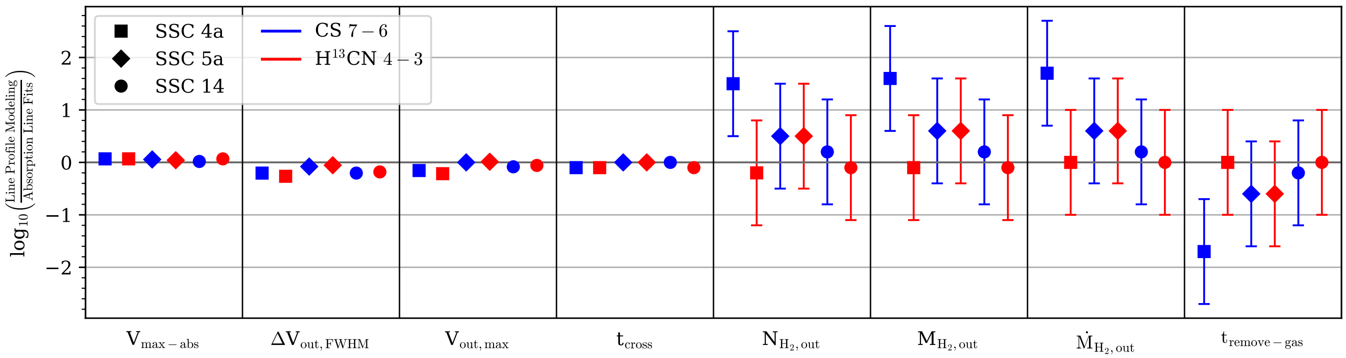

Figure 10. A comparison of common quantities measured from the absorption line fits (Section 3.1) and the line profile modeling (Section 3.2). Each bin (separated by black vertical lines) shows one quantity listed in Tables 2 and 3. Within the bins, points are artificially offset along the horizontal axis for clarity. The different symbols show the three SSCs and the colors show quantities derived from the two spectral lines, as defined in the legend. The vertical axis shows the logarithm of the ratio of the quantities from each method, such that each major tick mark corresponds to an order of magnitude. The error bars for the first four quantities are negligible; the errorbars on the last four quantities reflect the order-of-magnitude uncertainty on the abundance ratio of the molecule with respect to H_2.

mechanisms (4.2). We also investigate SSC 5a in more detail, as it is the only cluster visible in the NIR and shows evidence for a shell of dense gas surrounding it (4.3).

4.1. *Timescales, Ages, and Evolutionary Stages*

There are several timescales and ages calculated from this and previous analyses for these clusters, which we summarize here and list in Table 4:

ZAMS Age ($t_{ZAMS-age}$)—Rico-Villas et al. (2020) uses the ratio of the luminosity in protostars to that of ionizing zero-age main sequence (ZAMS) stars to estimate the ages of the clusters ($t_{ZAMS-age}$), finding that SSC 4a is $\sim 10^{4.95}$ yrs old, SSC 5a is $\gtrsim 10^5$ yrs old, and SSC 14 is $\sim 10^{4.88}$ yrs old (Table 4). These measurements are based on the same 36 GHz emission used by Leroy et al. (2018) to calculate the stellar masses. The stellar masses and ages associated with the ionizing photon rates derived from the ZAMS assumption may be underestimated if the cluster stellar population has evolved beyond the ZAMS stage, or if some fraction of the ionizing photons are absorbed by dust. These three SSCs have negligable synchrontron components of their SEDs, so synchrotron contamination of the 36 GHz emission is a small effect. These ages are, therefore, likely lower limits on the true "age" of the cluster.

Cluster Formation Timescales—Given the $t_{ZAMS-age}$ and free-fall times (t_{ff}) calculated by Leroy et al. (2018), we can try to place the clusters in a relative evolutionary sequence. An important caveat is that Leroy et al. (2018) estimated t_{ff} based on the marginally resolved data. With these spatially resolved data, the radii of the clusters decreased (e.g., Figure 11), meaning that these values of t_{ff} may be overestimated. SSCs 4a, 5a, and 14 have $t_{ZAMS-age}/t_{ff}$ = 1.1, $\gtrsim$2.0, and 2.4 respectively (Table 4). Modeling by Skinner & Ostriker (2015) suggests that gas is actively collapsing to form stars on timescales $\sim 1-2t_{ff}$, the typical timescale for cluster formation is $\sim 5t_{ff}$, and the gas is completely dispersed by $\sim 8t_{ff}$. These clusters should be nearing the end of the period of active gas collapse. SSC 5a may possibly be transitioning to the initial stages of gas dispersal, especially because it is the only cluster visible in the NIR (Section 4.3), though the gas dispersal has not yet finished because we still see evidence for an outflow. It is important to note, however, that these evolutionary stages are not clear-cut divisions, as gas accretion can continue while the cluster is forming and while outflows are present, and that the $t_{ZAMS-age}$ are likely lower limits on the cluster ages.

Crossing Time (t_{cross})—The crossing times (t_{cross}) we report in Tables 2 and 3 are short: $10^{4.5-5.2}$ years. Similarly short crossing times are also seen in a SSC candidate in the Large Magellanic Cloud ($\sim 10^{4.8}$ yr; Nayak et al. 2019) and in simulations (e.g. L. Lancaster et al., in prep.). At least one crossing-time has passed since the outflows turned on, as P-Cygni line profiles are detected out to $\gtrsim r_{SSC}$. If the outflows are present beyond r_{SSC}, they are increasingly difficult to detect in absorption away from the continuum source. Therefore, this timescale places a lower limit on the age of the outflow.

Gas Removal Time ($t_{remove-gas}$)—The gas removal times ($t_{remove-gas}$) are longer in general than the crossing or free-fall times, though the uncertainties on $t_{remove-gas}$ are large. The average $t_{remove-gas} \sim 10^{5.0\pm0.6}$ years, where the uncertainty is the standard deviation of the mean $t_{remove-gas}$ for each SSC and line. The gas removal times are $\gtrsim t_{ZAMS-age}$, except for SSC 4a. Assuming a constant mass outflow rate, this would imply that there is still gas in the clusters to be removed, though a constant mass outflow rate is unlikely (e.g. Kim et al. 2018).

Table 4. A comparison of relevant cluster timescales and ages

SSC Number	$\log_{10}(t_{ZAMS-age})^a$	$\log_{10}(t_{ff})^b$	$t_{ZAMS-age}/t_{ff}$	$\log_{10}(t_{cross})^c$	$\log_{10}(t_{remove-gas})^d$	$\log_{10}(t_{dep})^e$
4a	4.95	4.9	1.1	5.0	4.3±0.7	6.6
5a	$\gtrsim 5$	4.7	$\gtrsim$2.0	4.6	5.5±0.4	6.4
14	4.88	4.5	2.4	4.4	4.9±0.4	6.8

NOTE—For details, see the discussion in Section 4.1.

[a] The age of the cluster since the zero-age main sequence ($t_{ZAMS-age}$) calculated by the ratio of the luminosity in proto-stars to that in ZAMS stars from Rico-Villas et al. (2020).

[b] The free-fall time (t_{ff}) calculated by Leroy et al. (2018). For SSC 4a, the value for SSC 4 is used because SSC 4a is the dominant component of the SSC 4 complex. The uncertainty introduced by this assumption is likely minor compared to other uncertainties which are $\sim 0.4-0.5$ dex (c.f. Table 2 of Leroy et al. 2018).

[c] The time for gas to travel from the center of the cluster to the radius of the continuum source (r_{SSC}) at the typical outflow velocity ($V_{max-abs}$). This timescale (t_{cross}) is a proxy for the age of the outflow. For each SSC, this is the average of the values in Table 2 and 3.

[d] The time for the entire gas mass of the cluster (from Leroy et al. 2018) to be depleted at the current $\dot{M}_{H_2,outflow}$. For each SSC, this is the average of the values in Table 2 and 3. Uncertainties reported in the table are the standard deviations of the mean values from Table 2 and the values in Table 3. Propagated systematic uncertainties (due to the uncertainty in the molecular abundances) are 0.4 dex.

[e] The gas depletion timescale, defined as $t_{dep} \equiv \frac{M_{H_2,tot}}{SFR_{36\ GHz}}$. For SSC 4a, the gas mass for SSC 4 is used because SSC 4a is the dominant component of the SSC 4 complex.

Gas Depletion Timescale (t_{dep})—This timescale is the duration of future star formation, assuming a constant SFR for each cluster and no mass loss: $t_{dep} \equiv M_{H_2,tot}/SFR$ where $M_{H_2,tot}$ is from Leroy et al. (2018). The SFRs we use are also from Leroy et al. (2018) and are based on the measured 36 GHz fluxes which trace the free-free emission from each cluster (Gorski et al. 2017, 2019). This estimate of t_{dep} based on the SFR assumes continuous star formation (over $\sim$ 10 Myr; Murphy et al. 2011), whereas we would expect the actual star formation in these clusters to be bursty. These are the longest timescales for each cluster listed in Table 4. Compared to the clusters' $t_{ZAMS-age}$. This may suggest that the clusters are early in their star formation process and that there is plenty of fuel to form new stars and for the clusters to continue grow. This assumes, however, that all of the molecular gas remains in the cluster. The current gas removal times of the outflows ($t_{remove-gas}$) are much shorter than t_{dep}, indicating that these outflows will substantially affect the cluster's star formation efficiency (SFE).

That we detect outflows only in three sources, or $\sim$8% of the three dozen SSCs in the center of NGC 253 (Figure 1), gives credence to the idea that this outflowing phase must be short-lived. It is unlikely that we miss many sources with outflows due to their orientation and geometry because the modeling presented in Section 3.2 as well as simulations (e.g., Geen et al. 2020a) suggest that the outflows are wide. We could, however, be missing outflows if the outer layers of dense gas are very optically thick, which could obscure the outflows (e.g., Aalto et al. 2019) or if there are weak outflows below our sensitivity or cluster mass detection limits. Given that it is expected that the SSCs begin disrupting their natal clouds after $\sim 10^{5-6}$ years (Johnson et al. 2015) and taking $t_{cross} = 10^{4.5}$ years as the lower limit on the age of the outflow, we would expect to find outflows in at least 3−30% of SSCs, which agrees well with our detection rate of 8%. This percentile range is a lower limit because t_{cross} is the minimum possible age of the outflow and there could be additional outflows below our detection limit, though they would be weak. This also assumes that the clusters formed at the same time, which is also unlikely.

In general the chemistry-based age sequences presented by Krieger et al. (2020) lead to different relative cluster ages than the dynamical progression presented here, which are also different from the ZAMS age sequence of Rico-Villas et al. (2020). It is important to keep in mind, however, that the oldest clusters are not necessarily the most evolved, and vice versa. Using HCN/HC_3N as a relative age tracer, Krieger et al. (2020) suggest that SSCs 4 and 14 are in the younger half of the SSCs studied while SSC 5 is among the oldest. An age sequence using the chemistry of sulfur bearing molecules suggests instead that SSCs 5 and 14 are younger whereas SSC 4 is older (Krieger et al. 2020). This is in disagreement with the age progression suggested by Rico-Villas et al. (2020), who suggest an inside out formation with

SSCs 4–12 being the oldest and SSCs 1–3, 13, and 14 being the youngest. The detections of outflows towards SSCs 4a, 5a, and 14 would suggest that they are the most evolved clusters in the young burst, in the simplest model where the clusters completely and finally clear their gas at the end of their formation periods. As described in the following section, SSC 5a may be among the most evolved clusters, as it is the only one of these clusters visible in the NIR. Krieger et al. (2020) also find the lowest dense gas ratios in SSC 5a, suggesting that it has expelled and/or heated and dissociated much of its natal molecular gas. Given the gas-rich environment surrounding these clusters, however, it is possible that other clusters are older and more evolved, but have reaccreted gas from the surrounding medium or that was not completely expelled. Given that the mean velocities of the outflows in SSCs 4a, 5a, and 14 are less than the escape velocities, this is perhaps a likely scenario.

4.2. *Outflow Mechanics*

There are a handful of feedback mechanisms relevant for setting the SFE of star clusters. These include proto-stellar outflows, supernovae, photoionization, UV (direct) radiation pressure, dust-reprocessed (indirect) radiation pressure, and stellar winds. Each of these processes is efficient in driving outflows for different cluster masses, radii, and ages. One way to visualize this is through a mass-radius diagram (e.g., Fall et al. 2010; Krumholz et al. 2019), as shown in Figure 11. There is a locus where none of the feedback mechanisms considered by Krumholz et al. (2019) are efficient, and so clusters with those masses and radii should grow with high SFEs. An important caveat of this figure is that there are other parameters relevant to whether a feedback mechanism is efficient, such as the momentum carried by each mechanism and the timescales over which it operates, which are not shown in this representation.

We show in Figure 11 the primary SSCs in NGC 253, where SSCs without outflows are shown as circles and those with outflows are shown as diamonds. The radii are our measured half-flux radii listed in Table 1. Because of the factor of 4 improvement in the linear spatial resolution with respect to the observations reported by Leroy et al. (2018), the radii of these clusters are smaller than reported by Leroy et al. (2018). As a result, the clusters are systematically shifted down in Figure 11 as shown by the vertical dotted gray lines. The stellar masses (M_*) are from Leroy et al. (2018) based on the 36 GHz (free-free) luminosity for a ZAMS population with a standard initial mass function (IMF). There are several sources of uncertainty reflected in Figure 11. First, we assume that the primary clusters retain all of the stellar mass measured by Leroy et al. (2018), which may lead to an overestimate of M_* for those clusters that break apart. We estimate that this is at worst 50% in those cases (although the higher resolution data presented here shows a number of satellite structures, the original one remains dominant in most). Secondly, Leroy et al. (2018) estimate that there is a $\pm$20% systematic uncertainty due to assumptions about the Gaunt factor. Finally, E. A. C. Mills et al. (in prep.) measure M_* of these clusters at 5 pc resolution using hydrogen radio recombination lines (RRLs). These agree with the M_* estimated by Leroy et al. (2018) to within $\pm$0.3 dex on average. Included in the calculations by E. A. C. Mills et al. (in prep.) is the effect of a synchrotron component. If synchrotron contaminates the 36 GHz flux (which is assumed to be entirely free-free), this would lead to an overestimate of M_*. There is negligible synchrotron emission in SSCs 4a, 5a, and 14, but this could affect the M_* of other clusters (especially SSCs 1a, 10a, 11a, and 12a; E. A. C. Mills et al. in prep.). To determine the lower error bar on the M_* values plotted in Figure 11, we take the largest of the above three sources of uncertainty for each cluster, where the uncertainty from the RRL measurements are included only if they yield a smaller M_*. To determine the upper error bars, we take the larger of the 20% systematic uncertainty and RRL-measured M_* where they yield a larger M_*. In addition to these quantifiable uncertainties on M_*, there are unquantified uncertainties relating to ionizing photons absorbed by dust and evolution beyond the ZAMS, both of which would result in the reported stellar masses being underestimates (Leroy et al. 2018). While we do not show these unquantifiable uncertainties in Figure 11, we caution that they could be important.

Many of the SSCs in NGC 253 fall inside the white area of inefficient feedback in Figure 11, which suggests that none of those mechanisms may be efficient for these clusters. The detection of outflows in SSCs 4a, 5a, and 14, however, means there is direct evidence of strong feedback. The H_2 masses in the outflows are significant compared to the total mass in the cluster itself (Table 2). From the previous section (and quantified in Table 4), the gas removal times ($t_{remove-gas}$) based on the current mass outflow rates are much shorter than the timescale for future star formation (t_{dep}). Comparison of these timescales implies that the outflows will remove the molecular gas faster than it would otherwise be used up by star formation. Note that these timescales assume either a constant mass outflow rate or a constant star formation rate, respectively, neither of which is likely to be the case in reality. Moreover, $t_{remove-gas}$ assumes there is no new infall replenishing the reservoir, and t_{dep} assumes no molecular gas is removed. Nevertheless, the outflows will have a non-negligible effect on the reservoir of gas available to the cluster to form stars and hence on the cluster's SFE.

What mechanism, then, is powering these outflows, given that SSCs 4a and 5a lie in the locus where no mechanism is expected to be efficient and SSC 14 is near a boundary? We explore four plausible mechanisms shown in Figure 11 below

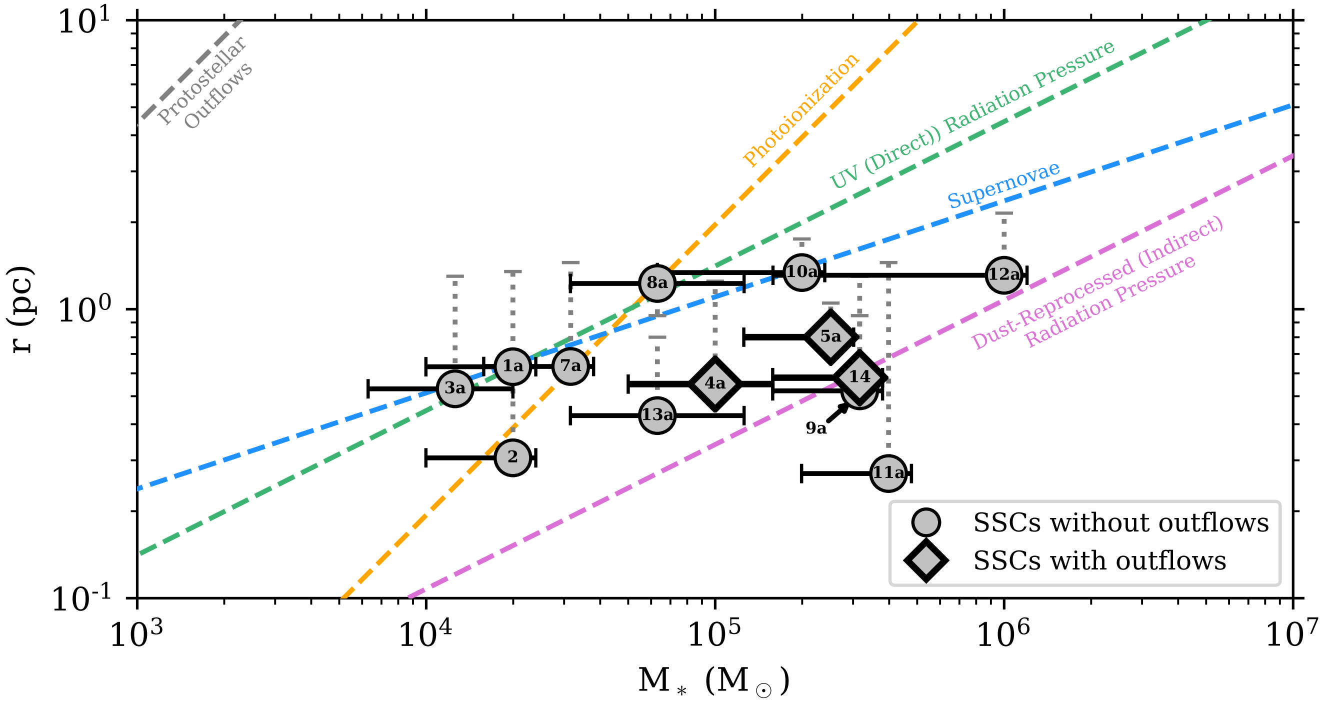

Figure 11. The cluster mass-radius diagram, adapted from Figure 12 of Krumholz et al. (2019). The colored shaded regions bounded by dashed lines show the regions of this parameter space where the corresponding feedback mechanism is efficient. There is a locus where none of these feedback mechanisms are expected to be efficient, resulting in high star formation efficiencies. The circles show the primary SSCs in NGC 253 without evidence for outflows, and the diamonds show those with outflows. The cluster stellar masses (M_*) are from Leroy et al. (2018). The error bars include differences with measurements from RRLs (E. A. C. Mills et al., in prep.), systematics due to assumptions about the Gaunt factor, and conservative estimates of the effects of the clusters resolving into multiple smaller clusters. Not shown are unquantified uncertainties related to absorption of ionizing photons by dust and evolution beyond the ZAMS, both of which would result in higher values of M_* than reported. See Section 4.2 for details on the calculation of the error bars. The radii are our measured 350 GHz half-flux radii (Table 1), which are smaller than the radii previously measured by Leroy et al. (2018) (horizontal gray line segments) due to the increase in the spatial resolution of these observations. The change in radius is shown by the vertical gray dotted lines. Notably, the SSCs with outflows lie within or near the locus where feedback is expected to be inefficient.

(excluding proto-stellar outflows which are only important for much lower mass clusters; e.g., Guszejnov et al. 2020). We also consider winds from high mass stars which may be important for clusters of these masses and ages (e.g., Gilbert & Graham 2007; Agertz et al. 2013; Geen et al. 2015, L. Lancaster et al. in prep.). In addition to their location in the mass-radius diagram (a re-framing of their surface densities), we also compare the momentum expected to be carried by each of these processes and the timescales over which they operate to the values estimated for these clusters. It is also possible that a synergistic combination of mechanisms is at work. These potential scenarios are discussed in the reminder of this section.

4.2.1. *Supernovae*

These clusters are young ($\sim 10^5$ years; Rico-Villas et al. 2020), and so it is not expected that many, if any, supernovae have exploded since it typically takes ∼3 Myr before the first supernova explosion. Moreover, the expected cloud lifetimes in a dense starburst like NGC 253 are expected to be shorter than 3 Myr (e.g., Murray et al. 2010), meaning that clouds would be disrupted before supernova feedback would be important. The gas removal times estimated for these outflows are $\ll 3$ Myr in all cases (Table 4), supporting the idea that the clusters are too young for supernovae. Even with the large uncertainties, the radial momentum we measure in their outflows (Table 2) is an order of magnitude or more lower than expected for supernova-driven outflows (1000-3000 km s^{-1}; e.g. Kim & Ostriker 2015; Kim et al. 2017a). Finally, E. A. C. Mills et al. (in prep.) construct millimeter spectral energy distributions of these SSCs at 5 pc resolution and find that all three of these sources have negligible synchrotron components, further ruling out supernovae as the mechanism driving the cluster outflows.

4.2.2. *Photoionization*

Photoionization can remove a substantial amount of gas from a cluster, depending primarily on the density of the cluster (e.g., Kim et al. 2018; He et al. 2019; Geen et al. 2020a,b; Dinnbier & Walch 2020). He et al. (2019) study the effects of photoionization on massive star clusters, finding that photoionization is most efficient at suppressing star formation in lower density clusters. Similarly, Dinnbier & Walch (2020) find that photoionization (and winds) are inefficient at clearing the natal gas from clusters with masses $> 5 \times 10^3$ $M_\odot$, unless they form with a high SFE. Though simulating different size and mass scales, Dinnbier & Walch (2020) and Geen et al. (2020a,b) find that feedback by photoionization is most important at the outer layers of the cloud or HII region. Kim et al. (2018) find that the momentum carried by a photoionization-driven outflow decreases with increasing cluster surface density. Assuming that the dense gas we measure follows the trends for the neutral gas simulated by Kim et al. (2018) and that the trends continue to these higher surface densities, the radial momentum per unit mass from photoionization should be very small ($p_r/M_* \lesssim 0.2$ km s^{-1}) for the molecular gas surface densities of SSCs 4a, 5a, and 14 of $\Sigma_{H_2} \sim 10^{4.4-5.3}$ $M_\odot$ pc^{-2} (Leroy et al. 2018). Using the stellar masses and radii, we can calculate the estimated ionized gas masses and momentum (using Equations 3, 4, and 11 of Leroy et al. 2018) and assuming $V_{ion} = 15$ km s^{-1} (as below), finding the $p_{ion}/M_* \approx 0.13,\ 0.15,$ and 0.08 km s^{-1} for SSCs 4a, 5a, and 14. We note that the ionizing photon rates estimated by Leroy et al. (2018) for these sources are consistent with a new analysis by E. A. C. Mills et al. (in prep.). These estimated momenta based on the ionizing photons are much smaller than the measured values of $p_r/M_* \approx 5-126,\ 1-3,$ and $5-40$ km s^{-1} (Table 2).

Krumholz et al. (2019) parameterize the effect of photoionizaion in terms of the ionized gas sound speed ($c_{s,ion}$) and the cluster escape velocity (V_{esc}), such that photoionization will be efficient when $c_{s,ion} > V_{esc}$. It is thought that the photoionization will be efficient for clusters with $V_{esc} \approx c_{s,ion} \leq 10$ km s^{-1}. Figure 11 and Krumholz et al. (2019) assume $V_{esc} \approx c_{s,ion} = 15$ km s^{-1}. The escape velocities of SSCs 4a, 5a, and 14 are approximately 23, 34, and 50 km s^{-1}, respectively. This suggests photoionization could be important for SSC 4a, but the escape velocities of SSCs 5a and 14 are likely too large for this mechanism to be efficient. This is in agreement with the qualitative results of simulations discussed above.

Therefore, feedback from photoionization likely plays a minor role in driving these outflows as these clusters are dense and hence their escape velocities are too large for photoionization to efficiently drive outflows.

4.2.3. *UV (Direct) Radiation Pressure*

There are many studies that investigate the role of UV (direct) radiation pressure in driving outflows and expelling gas from a molecular cloud or HII region (e.g., Kim et al. 2016, 2017b, 2018, 2019; Raskutti et al. 2017; Crocker et al. 2018a,b; Barnes et al. 2020; Dinnbier & Walch 2020). In general, many of these studies find that UV radiation pressure can play an important — if not dominant — role in expelling gas from a cluster, especially for low surface density clouds (e.g., Skinner & Ostriker 2015; Raskutti et al. 2017). Using a numerical radiation hydrodynamic approach, Raskutti et al. (2017) study the effects of radiation pressure from non-ionizing UV photons on massive star forming clouds, finding that over a cloud's lifetime $\gtrsim 50\%$ of the UV photons escape through low-opacity channels induced by turbulence and hence do not contribute to radiation pressure-driven outflows. An important caveat is that the clouds simulated by Raskutti et al. (2017) are larger in size and so have lower densities than the clusters in NGC 253. Raskutti et al. (2017) find that the mean outflow velocity of their radiation-pressure driven outflows is $\sim 1.5-2.5\ V_{esc}$, independent of cloud surface density. For the clusters in NGC 253, this translates to expected mean outflow velocities of $\sim 33-114$ km s^{-1}, faster than the observed mean velocities of $6-28$ km s^{-1}. The radial momentum per unit stellar mass (p_r/M_*) of SSCs 4a, 5a, and 14 are an order of magnitude or more less than measured by Raskutti et al. (2017) for clouds of roughly the same initial mass, though the clusters in NGC 253 are denser than the simulated clouds. In contrast, the clusters in NGC 253 have slightly larger radial momenta per unit outflowing mass (p_r/M_{out}). This means that the clusters in NGC 253 have less outflowing mass relative to their stellar masses than the simulated clusters, though this could also be due to the difference in cloud densities.

Simulations of feedback from photoionization and UV radiation pressure by Kim et al. (2018) find $t_{dep} \sim 2.5$ Myr for their densest clouds ($\Sigma_{neutral} = 10^3$ $M_\odot$ pc^{-2}). Our clusters, which have $\Sigma_{H_2} \sim 10^{4.4-5.3}$ $M_\odot$ pc^{-2} (Leroy et al. 2018), have $t_{dep}= 2.5-6.3$ Myr, whereas extrapolation of the Kim et al. (2018) calculations would result in lower values of t_{dep} if the trends continue to these higher densities. Kim et al. (2018) also find relatively constant outflow velocity of ~ 8 km s^{-1}, approximately independent of surface density in the neutral phase. This is similar to the mean outflow velocities of the dense gas traced by CS $7-6$ or $H^{13}CN$ $4-3$ for SSC 4a ($\approx$7 km s^{-1}), but lower than those for SSCs 5a and 14 ($\approx$ 22 and 25 km s^{-1}, respectively). In terms of momentum, according to Equation 18 in Kim et al. (2018), an outflow driven by photoionization and UV radiation pressure would have a momentum per unit stellar mass of ~ 1 km s^{-1} at the surface densities observed in our clusters. This is about an order of magnitude lower than the p_r/M_* measured for dense gas traced by CS $7-6$ or $H^{13}CN$ $4-3$ in these clusters (though our uncertainties are large). An important caveat to this is that the clusters in NGC 253 are denser than those simulated by Kim et al. (2018) and the simulations and observations probe different phases of the outflowing material (neutral and dense molecular respectively).

The efficiency of UV radiation pressure can be parameterized in terms of the surface mass density of the cluster (Σ) compared to the the outward force of radiation pressure. Skinner & Ostriker (2015) and Krumholz et al. (2019) define a critical surface density, $\Sigma_{\rm DR} = \frac{\Psi}{4\pi Gc}$ where Ψ is the light-to-mass ratio, below which UV radiation pressure becomes important. A population of ZAMS stars that fully samples a Chabrier (2003) IMF has $\Psi \approx 1100$ $L_\odot$ $M_\odot{}^{-1}$ (e.g. Fall et al. 2010; Kim et al. 2016; Crocker et al. 2018a), resulting in $\Sigma_{\rm DR} \approx 340$ $M_\odot$ pc^{-2}. Models and simulations show that UV radiation is only effective for surface densities $\Sigma \lesssim 10\,\Sigma_{\rm DR}$ because turbulence will introduce low-column sight-lines that allow the radiation to escape (e.g. Thompson & Krumholz 2016; Grudić et al. 2018; Krumholz et al. 2019). The value of $\Sigma_{\rm DR}$ depends principally and linearly on the assumed light-to-mass ratio and hence on the IMF. SSCs 4a, 5a, and 14 are all well below this boundary shown in green in Figure 11, meaning that a significantly top-heavy IMF resulting in a much higher value of Ψ is required for these outflows to be powered solely by UV radiation pressure. A top-heavy IMF has been suggested in other massive or super star clusters (e.g. Turner et al. 2017; Schneider et al. 2018). Turner et al. (2017) find a top-heavy IMF in a SSC in NGC 5253 with $\Psi \approx 2000$ $L_\odot$ $M_\odot^{-1}$. However, an unphysically large light-to-mass ratio $\sim 10,000$ $L_\odot$ $M_\odot^{-1}$ is needed for UV radiation to explain the feedback in SSCs 4a, 5a, and 14.

It is, therefore, unlikely that UV (direct) radiation pressure is the dominant mechanism responsible for driving the outflows in SSCs 4a, 5a, and 14.

4.2.4. *Dust-Reprocessed (Indirect) Radiation Pressure*

Given the large dust columns in these SSCs, dust-reprocessed (indirect) radiation pressure is a promising mechanism to power the outflows. In a study of massive star clusters in the Milky Way's Central Molecular Zone, Barnes et al. (2020) find that indirect radiation pressure is important at early times (< 1 Myr). Similarly, Olivier et al. (2020) find that dust-reprocessed radiation pressure is the dominant feedback mechanism in ultra compact HII regions in the Milky Way. Moreover, given the possible underestimate of the stellar masses due to absorption of ionizing photons by dust or evolution beyond the ZAMS (which are not reflected in the error bars in Figure 11), indirect radiation pressure is a plausible mechanism to drive the observed outflows.

Whether the dust-reprocessed radiation pressure can drive an outflow fundamentally depends on the balance between the outward force of the radiation pressure and the inward force of gravity (i.e. the Eddington ratio, $f_{\rm Edd}$). This depends on the dust opacity and the input luminosity from the cluster, which can be parameterized by the light-to-mass ratio of the assumed IMF. The dust opacity (κ_d) quantifies a dust grain's ability to absorb infrared radiation. As explored by Semenov et al. (2003), this quantity varies with temperature, dust composition, grain shape, grain size distribution, and the opacity model. For example, grains in dense molecular clouds exhibit larger κ_d than those in the diffuse ISM, which is thought to be due to the growth of mantles (e.g., Ossenkopf & Henning 1994). Given the high density and intense radiation environment in these clusters, the dust opacity may be quite different than found in Galactic regions, though we have no precise observational constraints on how much κ_d can vary in these environments. Often times, a dust-to-gas ratio (DGR) is assumed to convert the dust opacity to the opacity in the gas, and the standard Solar Neighborhood value is DGR = 0.01. Finally, the light-to-mass ratio (Ψ) depends on the assumed IMF, where a top-heavy IMF will have a larger value of Ψ. Top-heavy IMFs have been claimed in massive clusters with $\Psi \sim 2000$ $L_\odot$ $M_\odot^{-1}$ (e.g., Turner et al. 2017; Schneider et al. 2018) compared to either a Kroupa (2001) or Chabrier (2003) IMF which have $\Psi = 883$ $L_\odot$ $M_\odot^{-1}$ and $\Psi = 1100$ $L_\odot$ $M_\odot^{-1}$ respectively. Towards constraining the nature of the IMF in these clusters, E. A. C. Mills et al. (in prep.) measure the fraction of ionized helium towards these SSCs using H and He radio recombination lines at 5 pc resolution. This ratio is expected to be somewhat dependent on the IMF, as a top-heavy IMF will result in more massive stars capable of ionizing He. E. A. C. Mills et al. (in prep.) measure mass-weighted He^+ fractions which are consistent with He^+ fractions found in HII regions in the center of the Milky Way (e.g., Mezger & Smith 1976; de Pree et al. 1996; Lang et al. 1997) which is not thought to have a globally top-heavy IMF (e.g., Löckmann et al. 2010) though there are individual clusters which do seem to favor a top-heavy IMF (e.g., Lu et al. 2013). While the measured He^+ fractions do not completely rule out the possibility of a top-heavy IMF (it is unclear precisely how much the He^+ fraction changes with the IMF), it is unlikely that the IMF in these clusters is extremely top-heavy.

Below we describe two approaches taken by simulations in determining the efficiency of dust-reprocessed radiation pressure in driving outflows, and discuss how adjustments to the fiducal assumptions on κ_d, DGR, and Ψ may help explain the outflows observed in SSCs 4a, 5a, and 14.

Numerical simulations of dust-reprocessed radiation pressure by Skinner & Ostriker (2015) assume that the dust opacity (κ_d) is constant with temperature (and hence distance from the UV source). Skinner & Ostriker (2015) find:

$$f_{\rm Edd} = 0.68 \left(\frac{\rm DGR}{0.01}\right) \left(\frac{\kappa_d}{0.1\ {\rm cm^2\ g^{-1}}}\right) \left(\frac{\Psi}{883\ L_\odot\ M_\odot^{-1}}\right) \quad (4)$$

where we have explicitly included the dependence on the dust-to-gas ratio (DGR). For the fiducial values of DGR and Ψ, Skinner & Ostriker (2015) find $f_{\rm Edd} > 1$ only for

$\kappa_d > 0.15$ cm^2 g^{-1}, which is unphysically large for Solar Neighborhood-like dust properties (typically 0.03 cm^2 g^{-1}; Semenov et al. 2003). If, however, the dust is different in these environments than in the Solar Neighborhood, κ_d could be larger, though we have no observational constraints to evaluate this. Assuming Solar Neighborhood-like dust and a Kroupa (2001) IMF, we can achieve $f_{\rm Edd} > 1$ if DGR > 0.05. Although the center of NGC 253 is known to have a super-solar metallicity ($Z = 2.2 Z_\odot$; Davis et al. 2013) and the clusters may be even more dust-rich (Turner et al. 2015; Consiglio et al. 2016), a DGR > 0.05 seems quite high. Turning instead to the possibility of a top-heavy IMF, Equation 4 yields $f_{\rm Edd} > 1$ for $\Psi > 4300$ L$_\odot$ M$_\odot^{-1}$ (for Solar Neighborhood-like values of κ_d and DGR,), which is much more top-heavy than has been found in other SSCs (e.g., Turner et al. 2017). Given that E. A. C. Mills et al. (in prep.) do not find strong evidence for an increased He$^+$ fraction in these clusters, a very top-heavy IMF is unlikely. Finally, Skinner & Ostriker (2015) note that for clustered sources of UV photons — almost certainly the case in the SSCs in NGC 253 — there can be appreciable cancellation of the radiation pressure terms from each source, so that the net momentum to drive a cluster-scale outflow will be lower, independent of increases in the DGR, κ_d, or Ψ. Therefore, while there may be some combination of increased κ_d, DGR, and Ψ that enables dust-reprocessed radiation pressure to efficiently drive outflows in these clusters, it is unclear how much internal cancellation will affect the net momentum.

Crocker et al. (2018a) take a slightly different approach to study the efficiency of dust-reprocessed radiation pressure. From modeling of the Rosseland mean opacity by Semenov et al. (2003), $\kappa_d \propto T^2$ for $T < 100$ K. Crocker et al. (2018a) convert this temperature dependence into a radial dependence from the central source of UV photons, introducing a gradient in κ_d. This has the effect of boosting the effective dust opacity for clusters that are very dense, allowing for outflows to be driven more easily compared to Skinner & Ostriker (2015). Secondly, this allows Crocker et al. (2018a) to express their $f_{\rm Edd}$ in terms of a critical surface density:

$$\Sigma_{*,\rm IR} = \left(1.3\times10^5\ {\rm M_\odot\ pc^{-2}}\right) \times \left(\frac{\kappa_d}{0.03\ {\rm cm^2\ g^{-1}}}\right)^{-1} \left(\frac{\Psi}{1100\ {\rm L_\odot\ M_\odot}^{-1}}\right)^{-1} \left(\frac{\rm DGR}{0.01}\right)^{-1} \quad (5)$$

where we have again explicitly shown the dependence on the DGR. The dashed pink boundary in Figure 11 assumes the fiducial values of κ_d, Ψ, and DGR. While SSC 14 lies on this boundary, SSCs 4a and 5a fall above it, suggesting that dust-reprocessed radiation-pressure is not sufficient for driving outflows in these clusters.

Note, however, that there are considerable uncertainties in this picture. The cluster stellar masses may be underestimated if appreciable ionizing photons are absorbed by dust or if the stellar population is evolved beyond the ZAMS. Therefore, they may be closer to the region where dust-reprocessed radiation pressure is efficient than shown in Figure 11. Moreover, we do not fully understand the properties of dust in these conditions. As discussed above, the DGR in their surrounding gas may be $\gtrsim 0.022$ given the observed super-solar metallicity in the center of NGC 253 (Davis et al. 2013) and the high density conditions in the starburst molecular gas, which may favor dust formation. Assuming DGR = 0.022 in Equation 5, moves the $\Sigma_{*,\rm IR}$ boundary up to encompass SSCs 4a and 5a. This difference compared to the results of Skinner & Ostriker (2015) comes from the assumed temperature dependence in κ_d, which provides a boosted dust opacity for very compact sources. This itself is very uncertain, since the dust models are designed for proto-planetary disks, and the growth of κ_d with T saturates at $T \sim 100$ K (see Semenov et al. 2003). Considering changes to the IMF using the fiducial value of κ_d and the DGR would require $\Psi \gtrsim 3000$ L$_\odot$ M$_\odot^{-1}$ to explain SSCs 4a and 5a, or 1.5× more top-heavy than the IMF in NGC 5253 (Turner et al. 2017). Even with the boost in κ_d, there would still be cancellations in the radiation pressure due to clustered UV sources, although these cancellations may not be as severe as in the constant κ_d case.

Therefore, it is possible that dust-reprocessed (indirect) radiation pressure could drive the outflows observed in SSCs 4a, 5a, and 14, though this hinges critically on the behavior of the dust opacity (κ_d) for which there are no observational constraints in these extreme environments. A likely elevated dust-to-gas ratio (DGR) in these sources helps, but cancellations from clustered UV sources hinders the efficiency with which dust-reprocessed radiation pressure can drive outflows. Therefore, whether dust-reprocessed radiation plays a dominant role in powering the outflows observed from SSCs 4a, 5a, and 14 is an open question.

4.2.5. *Winds from High Mass Stars*

Given the stellar masses of these clusters ($M_* = 10^{5.0-5.5}$ M$_\odot$), we would expect $\gtrsim 1000-3000$ O stars in each cluster, assuming a Kroupa (2001) IMF. It has been suggested that outflows from young, massive SSCs in the Antennae are driven by a combination of O and Wolf Rayet (WR) stellar winds (Gilbert & Graham 2007), although other possible mechanisms are not evaluated. The combined power of the winds from these massive stars could, therefore, play an important role in powering the outflows from the clusters in NGC 253.

It has been suggested that winds from WR stars significantly impact how a cluster clears its natal gas, as they impart $\sim 10\times$ the energy of O-star winds over a shorter period of time (e.g., Sokal et al. 2016). The mass-loss rates of WR stars are metallicity dependent, with higher mass loss rates at higher metallicity for both carbon- and nitrogen-rich WR stars (Vink & de Koter 2005). Because WR stars are evolved O-stars, it is thought that they should not contribute much towards the cluster feedback until after $\sim 3-4$ Myr, when other processes such as supernovae are becoming important and when much of the natal gas has already been dispersed. In an observational study of massive embedded clusters, however, Sokal et al. (2016) find that WR winds are important even at earlier stages, though the clusters they study all have ages >1 Myr. Moreover, they find that clusters without WR stars tend to stay embedded longer than those with WR stars, indicating that WR winds may accelerate the gas-clearing stage.

It is unclear, however, whether the clusters in NGC 253 harbor WR stars yet, given their very young ages ($t_{\rm ZAMS-age} \approx 0.1$ Myr). There is evidence of a WR population towards SSC 5 — perhaps the most evolved cluster — but higher spatial and spectral resolution observations are needed to confirm this (Kornei & McCrady 2009; Davidge 2016). There is a known WR X-ray binary in NGC 253, but it is outside of the nuclear region studied here by ~ 250 pc in projection (Maccarone et al. 2014). Given the young ages of these clusters, it is unlikely that there are many, if any, WR stars present in these clusters, especially SSCs 4a and 14. Once a portion of the O star population evolves into WR stars, however, their winds could potentially strongly contribute to driving outflows.

Simulations of stellar wind feedback on the clearing of a cluster's natal gas have mixed conclusions. Some simulations show that stellar winds are important at early times in a cluster's life, especially for clearing the natal dense gas before supernovae start occurring at around 3 Myr (e.g., Agertz et al. 2013; Geen et al. 2015, 2020a,b). Given that the clusters in NGC 253 are substantially younger than this ($t_{\rm ZAMS-age} \approx 0.1$ Myr), stellar winds may be play a prominent role in driving the outflows we observe from these SSCs. Other simulations, however, find that stellar winds are most effective after 3 Myr (Calura et al. 2015). There are also simulations that find that stellar winds (and photoionization) alone cannot expel the natal gas for massive ($> 5\times10^3$ $M_\odot$) clusters at any time point unless they form with a SFE $\equiv M_*/(M_{\rm gas}+M_*) > 1/3$ (Dinnbier & Walch 2020).

In the absence of gas cooling, stellar winds can impart momentum into the surrounding material typically $p_r/M_* \approx 50-65$ km s^{-1} (Weaver et al. 1977), assuming a wind luminosity of 10^{34} erg s^{-1} (Starburst99; Leitherer et al. 1999), the ages of these clusters to be $\approx 10^5$ yrs (Rico-Villas et al. 2020), and $n_{\rm H} = 10^5$ cm^{-3}. These estimates are on the high side of our observed range of $p_r/M_* \approx 5-126$, $1-3$, and $5-40$ km s^{-1} for SSCs 4a, 5a, and 14 respectively (Table 2), and are fairly insensitive to the assumed average gas density (an order of magnitude in $n_{\rm H}$ results in a factor of ≈ 1.5 change in the expected momentum).

If the gas can cool, however, the momentum imparted will be substantially lower, and this is especially relevant in the large ambient densities found near these SSCs (e.g., Silich et al. 2004; Palouš et al. 2014; Wünsch et al. 2017; Lochhaas & Thompson 2017; El-Badry et al. 2019; Gray et al. 2019, L. Lancaster et al., in prep.). An outflow stalled by cooling has been claimed in a SSC in NGC 5253 (Cohen et al. 2018). Nonetheless, recent simulations by L. Lancaster et al. (in prep.) find that although cooling is important for the gas densities in the central starburst of NGC 253, the momentum imparted before cooling still provides a modest enhancement over a momentum-conserving wind. The computed enhancement factor (α_p) is sufficient to power outflows even with efficient cooling (with $\alpha_p \approx 1-4$). For the typical ages of these SSCs (~ 0.1 Myr), L. Lancaster et al. (in prep.) predict a momentum injection of $p_r/M_* \approx 0.8$ km s^{-1}, lower than momenta measured for SSCs 4a, 5a, and 14 of $p_r/M_* \approx 5-126$, $1-3$, and $5-40$ km s^{-1} (Table 2). Given the predicted shell velocity from L. Lancaster et al. (in prep.), we can estimate the value of α_p implied by the observed outflows:

$$\alpha_p = \left(\frac{V_{\rm max-abs}}{2.0\ {\rm km\ s^{-1}}}\right)^2 \left(\frac{M_{\rm H_2,out}}{M_*}\right) \left(\frac{r_{\rm SSC}}{1\ {\rm pc}}\right)^{-1}. \quad (6)$$

For the measured outflow properties of SSCs 4a, 5a, and 14, this suggests $\alpha_p \approx 9-227$, $4-10$, and $34-272$ respectively (using the parameters in Tables 1 and 2). Given the uncertainties in our masses it is certainly possible that the outflow in 5a is powered by stellar winds. Given the concerns about saturation in SSC 4a, the outflowing mass may be overestimated and so our calculated α_p may also be overestimated, which makes it also possible for it to be due to stellar winds. For all SSCs, given that our values of M_* may be underestimated, this would also reduce the value of α_p. For SSC 14, this is unlikely to be sufficient to explain its outflow solely by stellar winds.

Therefore, O star winds are unlikely to be driving the outflow observed towards SSC 14 in NGC 253, although it is possible they play a role in driving the current outflows in SSCs 4a and 5a, especially if the current stellar masses of these clusters are underestimated. The O star populations in these clusters are likely too young to host many WR stars, except perhaps in the case of SSC 5a, so the effect of WR star winds is likely negligible at this stage in the SSCs evolution.

4.2.6. *Summary: What Mechanisms Power the Outflows?*

To summarize the above exploration of possible feedback mechanisms, we find that the outflows from SSCs 4a, 5a, and 14 are difficult to explain, though they are likely powered by a combination of dust-reprocessed radiation pressure and stellar winds. All three clusters are too young for supernovae to have exploded and too dense for photoionization or UV (direct) radiation pressure to be efficient. Whether dust-reprocessed radiation pressure is efficient depends on the properties of the dust opacity (κ_d), for which there are virtually no constraints in extreme environments like these SSCs, and likely requires some combination of a higher dust opacity, an increased dust-to-gas-ratio, and a top-heavy IMF, all of which are currently poorly constrained in these clusters. Moreover, clustered UV sources within the SSCs can have the effect of cancelling out the radiation pressure terms from other sources (Skinner & Ostriker 2015), reducing the net momentum to drive a cluster-scale outflow. In the case of stellar winds, cooling is expected to be important for these clusters. Although recent simulations find that even in the presence of strong cooling O star stellar winds may be sufficient to power outflows (L. Lancaster et al. in prep.), we find that the expected momentum is insufficient to explain the observed properties of the outflows in SSC 14 and possibly in SSC 4a. For SSC 14, the outflows are likely dominated by dust-reprocessed radiation pressure, whereas the outflow in SSC 5a may be dominated by stellar winds. For SSC 4a, the deep absorption renders the outflowing mass estimate especially uncertain and likely overestimated, so we can only say that the outflow in that cluster is likely a combination of dust-reprocessed radiation pressure and stellar winds. Therefore, the precise mechanism(s) powering these outflows remains uncertain.

4.3. *SSC 5a and HST NIR Clusters*

Several clusters and one SSC have been previously identified in the center of NGC 253 based on *HST* near-infrared (NIR) images (Watson et al. 1996; Kornei & McCrady 2009), with the NIR-detected SSC corresponding to SSC 5 (Leroy et al. 2018). To be able to see the NIR emission, the cluster must have dispersed much of its natal gas and dust or it aligns with a serendipitous hole in the extinction screen. If the presence of NIR emission at this cluster location is from gas clearing, this implies that the cluster must be older than the other, highly extincted clusters. As shown in Figure 6, we see evidence for a weak outflow in the dense gas tracers from this cluster, which may be the tail-end of this gas dispersal process from the timescale arguments in Section 4.1. The measured mass outflow rate and momentum injection are also lower than for SSCs 4a and 14. It is important to note, however, that SSC 5a still has a high overall gas fraction ($M_{H_2,tot}/M_*$) of 0.8, though it is not as high as SSCs 4a and 14 (1.3 and 1.6, respectively).

Further support for this picture comes from the discovery of a shell near SSC 5a in HCN $4-3$ as shown in Figure 12. This feature is too faint to be seen in CS $7-6$ or $H^{13}CN$ $4-3$ at this resolution. The shell is visible from $\sim 35-70$ km s^{-1} relative to the cluster systemic velocity (Table 1) and has a projected radius of ~ 6 pc, though it is not perfectly centered on SSC 5a. Using these projected velocities, this implies an age of $\sim 8-16\times10^4$ years. At its largest extent, the shell reaches the location of SSC 4a (in projection) which also has a dense gas outflow. This shell-like structure is not seen around any other SSCs.

Kornei & McCrady (2009) note that the Pa-α emission around SSC 5a is asymmetric (Figure 12) and could be indicative of an outflow. We investigate how this asymmetric geometry corresponds to the observed shell in HCN $4-3$. There are systematic offsets between the location of SSC 5a in the ALMA data, the NIR clusters identified in the *HST* NICMOS data by Watson et al. (1996), and the F187N and F190N *HST* NICMOS data used by Kornei & McCrady (2009). Leroy et al. (2018) corrected the positions of the Watson et al. (1996) NIR clusters by $\Delta\alpha,\ \Delta\delta = +0.32'',\ -0.5''$, so that the NIR cluster corresponding to SSC 5a has $\alpha,\ \delta$ = $00^h47^m32.985^s$, $-25^\circ17^m19.76^s$ (J2000). The positions of the F187N and F190N mosaics[4] were corrected by matching the locations of the NIR clusters identified by Watson et al. (1996). A linear shift of $\Delta\alpha,\ \Delta\delta = +1.48'',\ -0.85''$ brings the *HST* images into agreement with the NIR clusters and the ALMA datasets. Figure 12 shows the Pa-α (F187N-F190N) image around SSC 5a with the HCN $4-3$ contours overlaid. The expanding HCN $4-3$ shell is not particularly aligned with the asymmetry seen in the Pa-α emission, though it does seem to align with the north-western edge.

The inferred mass of SSC 5a from the NIR emission ranges from $\geq 1.5\times10^6$ M$_\odot$ (Watson et al. 1996, who assume a Salpeter IMF from 0.08 M$_\odot$–100 M$_\odot$) to $1.4^{+0.4}_{-0.5}\times10^7$ M$_\odot$ (Kornei & McCrady 2009, who assume a Kroupa IMF). Leroy et al. (2018) calculate the ZAMS mass needed to produce the 36 GHz emission through free-free emission of $\sim 2.5\times10^5$ M$_\odot$. This is a lower-limit for several reasons. First, this mass estimate does not account for absorption due to dust, which may be significant, in which case we are only counting a fraction of the true free-free emission and hence the stellar mass. Secondly, if the cluster is more evolved — as we expect SSC 5a to be — the ZAMS mass will be an underestimate. Moreover, the estimate by Leroy et al. (2018) considered only the compact 36 GHz flux centered on the cluster: the fact that the Pa-α recombination is more extended suggests that considerable flux was missed in the radio observations. The fact that the mass estimates from the NIR are

[4] These calibrated and reduced *HST* NICMOS (NIC2) images were downloaded from the Mikulski Archive for Space Telescopes (MAST) database from M. Rieke's August 1998 program with exposure times of $\approx$384 s. The mosaic tiles were stitched together using the `reproject` package in Astropy.

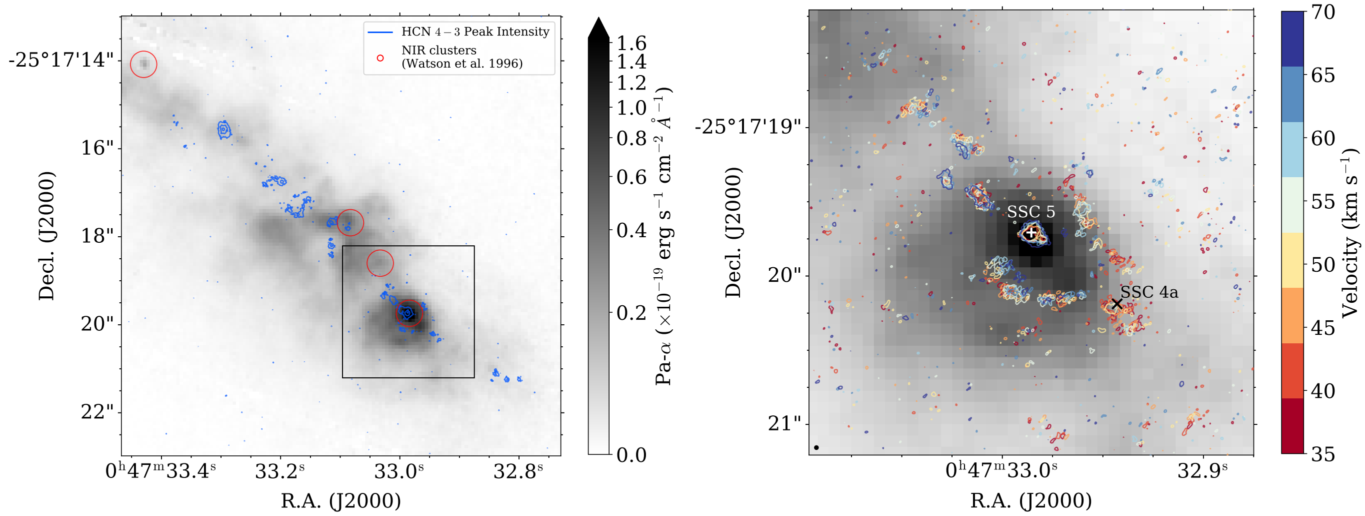

Figure 12. (Left) The *HST* Pa-α image. The blue contours show the ALMA HCN $4-3$ peak intensity at 2, 5, and $10\times$ the rms of the peak intensity image. The red circles show the NIR clusters identified by Watson et al. (1996), where the size of the circle reflects their $0.3''$ positional uncertainty. Only one of the primary clusters (SSC 5a) corresponds to the previously identified NIR clusters. (Right) The *HST* Pa-α image centered on SSC 5a (white plus sign) over the $3''\times3''$ black square from the left panel. There is an asymmetry in the Pa-α emission, which Kornei & McCrady (2009) posit may be due to an outflow. The contours show the HCN $4-3$ emission in selected the velocity channels relative to the systemic velocity of SSC 5a (Table 2) showing a shell-like structure with a velocity gradient across the shell. The contours are drawn at $3\times$ the rms of the HCN $4-3$ cube. The location of SSC 4a is also marked for context (black cross). The asymmetry in the Pa-α emission does not align with the HCN $4-3$ shell. This shell of HCN $4-3$ may be the signature of an earlier (stronger) outflow phase from SSC 5a.

$1-2$ orders of magnitude larger strongly suggest that one or more of these possibilities apply.

It is therefore possible that this shell is a previous (stronger) version of the outflow detected spectrally in this work. The shell age of $\sim10^5$ years is in good agreement with the minimum ZAMS age and the end of the period of active gas accretion (Section 4.1). It is unlikely that the outflow is due to a supernova explosion both because synchrotron emission is a negligible component of SSC 5's spectral energy distribution (E. A. C. Mills et al., in prep) and because the current momentum injection is well below what is expected from supernovae (e.g. Kim & Ostriker 2015; Kim et al. 2017a).

5. SUMMARY

The central starburst in NGC 253 harbors over a dozen massive ($M_* \sim 10^5$ M$_\odot$, a likely lower limit inferred from radio recombination lines and radio continuum) and extremely young star clusters which are still very rich in gas and likely in the process of formation (Leroy et al. 2018, E. A. C. Mills et al. in prep.). Using high resolution ($\theta \approx 0.028''$, equivalent to 0.48 pc) data from ALMA we study the 350 GHz (0.85 mm) spectra of these objects. We summarize our main results below, indicating the relevant figures and/or tables.

1. We observe P-Cygni line profiles — indicative of outflowing gas — in three super star clusters in the center of NGC 253, sources 4a, 5a, and 14 (c.f., Table 1). These line profiles can be seen in the full-band spectra in many lines (Figure 3), and particularly cleanly in the CS $7-6$ and H^{13}CN $4-3$ lines which are the focus of this analysis (Figures 1 and 6). Among these clusters, 5a is notable for being the only one of the massive clusters that is observable in the near IR (Figure 12), suggesting it has cleared much of its surrounding gas.

2. By fitting the absorption line profiles (Figure 6), we measure outflow velocities, column densities, masses, and mass outflow rates (Table 2). The outflow crossing times — a lower limit on the outflow age — are short ($\sim$ few $\times\,10^4$ yr), suggesting we are witnessing a short-lived phase. The outflowing mass in these objects is a non-negligible fraction of the total gas or stellar mass.

3. To place limits on the opening angles and line of sight orientations of the outflows we construct a simple radiative transfer model aiming at reproducing the observed P-Cygni profiles in CS $7-6$ and H^{13}CN $4-3$ (Figures 7 and 8). By varying the input temperatures, densities, velocities, and velocity dispersion of each component as well as the opening angle and orientation of the outflow component, we find that very wide opening angle models best reproduce the observed P-Cygni profiles (Figure 6). While we cannot precisely determine the opening angle for each cluster, the outflows must be almost spherical, although somewhat

smaller opening angles are acceptable if the outflows are pointed almost perfectly along the line of sight (Figure 9). This modeling also provides measurements of the outflow velocity, column density, masses, and mass outflow rates (Table 3). In general, these two sets of measurements agree, given the large uncertainties (Figure 10).

4. We compare measurements of the ZAMS age (Rico-Villas et al. 2020) to the gas free-fall time (Leroy et al. 2018), outflow crossing time, gas removal time implied by the mass outflow rate, and the gas depletion time (Table 4). These estimates are consistent with the SSCs still being in a period of active gas collapse, though SSC 5a could be past this phase. The gas removal timescale (assuming a constant mass outflow rate) is about an order of magnitude smaller than the gas depletion time due to star formation, showing that the outflows will have a substantial effect on the star formation efficiency of these SSCs.

5. Given our measured velocities, masses, radii, surface densities, and momentum per unit stellar mass, we investigate the mechanisms responsible for driving the observed outflows. Possibilities are supernovae, photoionization, UV (direct) radiation pressure, dust-reprocessed (indirect) radiation pressure, and O star stellar winds. While none of these mechanisms completely explains the observations, the two explanations that are potentially in play are dust-reprocessed radiation pressure and stellar winds. It is possible that the outflows are powered by a combination of both mechanisms, with the feedback in SSC 14 dominated by dust-reprocessed radiation pressure and the feedback in SSC 5a dominated by stellar winds (Figure 11, Section 4.2).

6. We report the discovery of an expanding shell (seen in HCN 4 − 3) around SSC 5a with $r \sim 6$ pc (Figure 12). As mentioned above, SSC 5a is the only cluster visible in the near IR, which coupled with it having only a lower limits on the ZAMS age suggests that SSC 5a is the most evolved cluster. SSC 5a also has the weakest P-Cygni profile among the three detected and the smallest current mass outflow rate. Given its velocity and size, the shell is $\sim 10^5$ yrs old, in good agreement with the minimum ZAMS age of the cluster and estimates of the end of the period of active gas collapse (Table 4). It is thus likely that the expanding shell is a remnant from the earlier stages of the gas clearing phase when the outflow was stronger. It is unlikely that this shell was created by a past supernova explosion as synchrotron emission is a negligible component of this cluster's spectral energy distribution on 5 pc scales (E. A. C. Mills et al. in prep.).

While the SSCs in the heart of NGC 253 constitute a very young population of clusters, there is evidence for differing evolutionary stages among them. A major step towards better characterizing these clusters is better measurements of their stellar masses. Current stellar mass estimates use the 36 GHz continuum emission — assuming that it is all due to free-free emission — to calculate the ionizing photon rate and hence the stellar mass (Leroy et al. 2018). Due to the enormous extinctions towards these clusters, it is not feasible to use traditional optical and near IR recombination lines as tracers of the ionized gas. High resolution hydrogen radio recombination lines (RRLs) offer direct probes of the ionizing photon rate and hence the stellar mass, and are uninhibited by dust extinction (Emig et al. 2020 in NGC 4945, E. A. C. Mills et al. in prep. in NGC 253). In the near future, *James Webb Space Telescope* observations may allow us to independently establish stellar masses and radiation fields by accessing mid IR spectral line indicators. In the next decade, the combination of sensitivity and exquisite resolution of the Next Generation Very Large Array (ngVLA) may make studies at this high resolution possible for galaxies out to the Virgo cluster and beyond.

ACKNOWLEDGMENTS

R.C.L. thanks Eve Ostriker for very helpful discussions and feedback which greatly improved this paper. R.C.L. also thanks Todd Thompson and Stuart Vogel for useful conversations and advice. The authors thank Nicolas Bolatto for his help in making the 3D visualizations for Figures 8 and B1. R.C.L. acknowledges support for this work provided by the NSF through Student Observing Support Program (SOSP) award 7-011 from the NRAO. K.L.E. acknowledges financial support from the Netherlands Organization for Scientific Research through TOP grant 614.001.351. This paper makes use of the following ALMA data: ADS/JAO.ALMA#2017.1.00433.S. ALMA is a partnership of ESO (representing its member states), NSF (USA) and NINS (Japan), together with NRC (Canada), MOST and ASIAA (Taiwan), and KASI (Republic of Korea), in cooperation with the Republic of Chile. The Joint ALMA Observatory is operated by ESO, AUI/NRAO and NAOJ. E.R. acknowledges the support of the Natural Sciences and Engineering Research Council of Canada (NSERC), funding reference number RGPIN-2017-03987. The National Radio Astronomy Observatory is a facility of the National Science Foundation operated under cooperative agreement by Associated Universities, Inc. Based on observations made with the NASA/ESA Hubble Space Telescope, obtained from the data archive at the Space Telescope Science Institute. STScI is operated by the Association of Universities for Research in Astronomy, Inc. under NASA contract NAS 5-26555.

Facilities: ALMA, HST

Software: Astropy (The Astropy Collaboration et al. 2018), CASA (McMullin et al. 2007), `emcee` (Foreman-Mackey et al. 2013), MatPlotLib (Barrett et al. 2005), NumPy (Harris et al. 2020), pandas (McKinney 2010), photutils (Bradley et al. 2018), SciPy (Jones et al. 2001–), seaborn (Waskom et al. 2014)

REFERENCES

Aalto, S., Muller, S., König, S., et al. 2019, A&A, 627, A147, doi: 10.1051/0004-6361/201935480

Agertz, O., Kravtsov, A. V., Leitner, S. N., & Gnedin, N. Y. 2013, ApJ, 770, 25, doi: 10.1088/0004-637X/770/1/25

Anantharamaiah, K. R., & Goss, W. M. 1996, ApJL, 466, L13, doi: 10.1086/310157

Ando, R., Nakanishi, K., Kohno, K., et al. 2017, ApJ, 849, 81, doi: 10.3847/1538-4357/aa8fd4

Barnes, A. T., Longmore, S. N., Dale, J. E., et al. 2020, MNRAS, doi: 10.1093/mnras/staa2719

Barrett, P., Hunter, J., Miller, J. T., Hsu, J.-C., & Greenfield, P. 2005, in Astronomical Society of the Pacific Conference Series, Vol. 347, Astronomical Data Analysis Software and Systems XIV, ed. P. Shopbell, M. Britton, & R. Ebert, 91

Bendo, G. J., Beswick, R. J., D'Cruze, M. J., et al. 2015, MNRAS, 450, L80, doi: 10.1093/mnrasl/slv053

Bradley, L., Sipőcz, B., Robitaille, T., et al. 2018, astropy/photutils: v0.5, doi: 10.5281/zenodo.1340699

Calura, F., Few, C. G., Romano, D., & D'Ercole, A. 2015, ApJL, 814, L14, doi: 10.1088/2041-8205/814/1/L14

Chabrier, G. 2003, PASP, 115, 763, doi: 10.1086/376392

Charnley, S. B. 1997, ApJ, 481, 396, doi: 10.1086/304011

Cohen, D. P., Turner, J. L., Consiglio, S. M., Martin, E. C., & Beck, S. C. 2018, ApJ, 860, 47, doi: 10.3847/1538-4357/aac170

Colzi, L., Fontani, F., Caselli, P., et al. 2018, A&A, 609, A129, doi: 10.1051/0004-6361/201730576

Consiglio, S. M., Turner, J. L., Beck, S., & Meier, D. S. 2016, ApJL, 833, L6, doi: 10.3847/2041-8205/833/1/L6

Cordoni, G., Milone, A. P., Mastrobuono-Battisti, A., et al. 2020, in IAU Symposium, Vol. 351, IAU Symposium, ed. A. Bragaglia, M. Davies, A. Sills, & E. Vesperini, 281–284, doi: 10.1017/S1743921319007737

Crocker, R. M., Krumholz, M. R., Thompson, T. A., Baumgardt, H., & Mackey, D. 2018a, MNRAS, 481, 4895, doi: 10.1093/mnras/sty2659

Crocker, R. M., Krumholz, M. R., Thompson, T. A., & Clutterbuck, J. 2018b, MNRAS, 478, 81, doi: 10.1093/mnras/sty989

Davidge, T. J. 2016, ApJ, 818, 142, doi: 10.3847/0004-637X/818/2/142

Davis, T. A., Bayet, E., Crocker, A., Topal, S., & Bureau, M. 2013, MNRAS, 433, 1659, doi: 10.1093/mnras/stt842

de Pree, C. G., Gaume, R. A., Goss, W. M., & Claussen, M. J. 1996, ApJ, 464, 788, doi: 10.1086/177364

Dinnbier, F., & Walch, S. 2020, MNRAS, 499, 748, doi: 10.1093/mnras/staa2560

Draine, B. T. 2011, Physics of the Interstellar and Intergalactic Medium

El-Badry, K., Ostriker, E. C., Kim, C.-G., Quataert, E., & Weisz, D. R. 2019, MNRAS, 490, 1961, doi: 10.1093/mnras/stz2773

Emig, K. L., Bolatto, A. D., Leroy, A. K., et al. 2020, arXiv e-prints, arXiv:2009.05154. https://arxiv.org/abs/2009.05154

Fall, S. M., Krumholz, M. R., & Matzner, C. D. 2010, ApJL, 710, L142, doi: 10.1088/2041-8205/710/2/L142

Foreman-Mackey, D., Hogg, D. W., Lang, D., & Goodman, J. 2013, PASP, 125, 306, doi: 10.1086/670067

Geen, S., Bieri, R., Rosdahl, J., & de Koter, A. 2020a, arXiv e-prints, arXiv:2009.08742. https://arxiv.org/abs/2009.08742

Geen, S., Hennebelle, P., Tremblin, P., & Rosdahl, J. 2015, MNRAS, 454, 4484, doi: 10.1093/mnras/stv2272

Geen, S., Pellegrini, E., Bieri, R., & Klessen, R. 2020b, MNRAS, 492, 915, doi: 10.1093/mnras/stz3491

Gilbert, A. M., & Graham, J. R. 2007, ApJ, 668, 168, doi: 10.1086/520910

Ginsburg, A., & Kruijssen, J. M. D. 2018, ApJ, 864, L17, doi: 10.3847/2041-8213/aada89

Gorski, M., Ott, J., Rand, R., et al. 2017, ApJ, 842, 124, doi: 10.3847/1538-4357/aa74af

Gorski, M. D., Ott, J., Rand, R., et al. 2019, MNRAS, 483, 5434, doi: 10.1093/mnras/sty3077

Gray, W. J., Oey, M. S., Silich, S., & Scannapieco, E. 2019, ApJ, 887, 161, doi: 10.3847/1538-4357/ab510d

Grudić, M. Y., Hopkins, P. F., Faucher-Giguère, C.-A., et al. 2018, MNRAS, 475, 3511, doi: 10.1093/mnras/sty035

Guszejnov, D., Grudić, M. Y., Hopkins, P. F., Offner, S. S. R., & Faucher-Giguère, C.-A. 2020, arXiv e-prints, arXiv:2010.11249. https://arxiv.org/abs/2010.11249

Harris, C. R., Millman, K. J., van der Walt, S. J., et al. 2020, Nature, 585, 357, doi: 10.1038/s41586-020-2649-2

He, C.-C., Ricotti, M., & Geen, S. 2019, MNRAS, 489, 1880, doi: 10.1093/mnras/stz2239

Henkel, C., Asiri, H., Ao, Y., et al. 2014, A&A, 565, A3, doi: 10.1051/0004-6361/201322962

Herrera, C. N., & Boulanger, F. 2017, A&A, 600, A139, doi: 10.1051/0004-6361/201628454

Johnson, K. E., Leroy, A. K., Indebetouw, R., et al. 2015, ApJ, 806, 35, doi: 10.1088/0004-637X/806/1/35

Johnson, L. C., Seth, A. C., Dalcanton, J. J., et al. 2016, ApJ, 827, 33, doi: 10.3847/0004-637X/827/1/33

Jones, E., Oliphant, T., Peterson, P., et al. 2001–, SciPy: Open source scientific tools for Python. http://www.scipy.org/

Kamann, S., Bastian, N. J., Gieles, M., Balbinot, E., & Hénault-Brunet, V. 2019, MNRAS, 483, 2197, doi: 10.1093/mnras/sty3144

Kim, C.-G., & Ostriker, E. C. 2015, ApJ, 802, 99, doi: 10.1088/0004-637X/802/2/99

Kim, C.-G., Ostriker, E. C., & Raileanu, R. 2017a, ApJ, 834, 25, doi: 10.3847/1538-4357/834/1/25
Kim, J.-G., Kim, W.-T., & Ostriker, E. C. 2016, ApJ, 819, 137, doi: 10.3847/0004-637X/819/2/137
—. 2018, ApJ, 859, 68, doi: 10.3847/1538-4357/aabe27
—. 2019, ApJ, 883, 102, doi: 10.3847/1538-4357/ab3d3d
Kim, J.-G., Kim, W.-T., Ostriker, E. C., & Skinner, M. A. 2017b, ApJ, 851, 93, doi: 10.3847/1538-4357/aa9b80
Koribalski, B. S., Staveley-Smith, L., Kilborn, V. A., et al. 2004, AJ, 128, 16, doi: 10.1086/421744
Kornei, K. A., & McCrady, N. 2009, ApJ, 697, 1180, doi: 10.1088/0004-637X/697/2/1180
Krieger, N., Bolatto, A. D., Walter, F., et al. 2019, ApJ, 881, 43, doi: 10.3847/1538-4357/ab2d9c
Krieger, N., Bolatto, A. D., Leroy, A. K., et al. 2020, ApJ, 897, 176, doi: 10.3847/1538-4357/ab9c23
Kroupa, P. 2001, MNRAS, 322, 231, doi: 10.1046/j.1365-8711.2001.04022.x
Kruijssen, J. M. D. 2012, MNRAS, 426, 3008, doi: 10.1111/j.1365-2966.2012.21923.x
Krumholz, M. R., McKee, C. F., & Bland -Hawthorn, J. 2019, ARA&A, 57, 227, doi: 10.1146/annurev-astro-091918-104430
Lang, C. C., Goss, W. M., & Wood, O. S. 1997, ApJ, 474, 275, doi: 10.1086/303452
Leitherer, C., Schaerer, D., Goldader, J. D., et al. 1999, ApJS, 123, 3, doi: 10.1086/313233
Leroy, A. K., Bolatto, A. D., Ostriker, E. C., et al. 2015, ApJ, 801, 25, doi: 10.1088/0004-637X/801/1/25
—. 2018, ApJ, 869, 126, doi: 10.3847/1538-4357/aaecd1
Lochhaas, C., & Thompson, T. A. 2017, MNRAS, 470, 977, doi: 10.1093/mnras/stx1289
Löckmann, U., Baumgardt, H., & Kroupa, P. 2010, MNRAS, 402, 519, doi: 10.1111/j.1365-2966.2009.15906.x
Lu, J. R., Do, T., Ghez, A. M., et al. 2013, ApJ, 764, 155, doi: 10.1088/0004-637X/764/2/155
Maccarone, T. J., Lehmer, B. D., Leyder, J. C., et al. 2014, MNRAS, 439, 3064, doi: 10.1093/mnras/stu167
Mangum, J. G., & Shirley, Y. L. 2015, PASP, 127, 266, doi: 10.1086/680323
Mapelli, M. 2017, MNRAS, 467, 3255, doi: 10.1093/mnras/stx304
Martín, S., Aladro, R., Martín-Pintado, J., & Mauersberger, R. 2010, A&A, 522, A62, doi: 10.1051/0004-6361/201014972
Martín, S., Mauersberger, R., Martín-Pintado, J., Henkel, C., & García-Burillo, S. 2006, ApJS, 164, 450, doi: 10.1086/503297
Martín, S., Muller, S., Henkel, C., et al. 2019, A&A, 624, A125, doi: 10.1051/0004-6361/201935106
McKinney, W. 2010, in Proceedings of the 9th Python in Science Conference, ed. S. van der Walt & J. Millman, 51 – 56
McMullin, J. P., Waters, B., Schiebel, D., Young, W., & Golap, K. 2007, in Astronomical Society of the Pacific Conference Series, Vol. 376, Astronomical Data Analysis Software and Systems XVI, ed. R. A. Shaw, F. Hill, & D. J. Bell, 127
Meier, D. S., Walter, F., Bolatto, A. D., et al. 2015, ApJ, 801, 63, doi: 10.1088/0004-637X/801/1/63
Mezger, P. G., & Smith, L. F. 1976, A&A, 47, 143
Murphy, E. J., Condon, J. J., Schinnerer, E., et al. 2011, ApJ, 737, 67, doi: 10.1088/0004-637X/737/2/67
Murray, N., Quataert, E., & Thompson, T. A. 2010, ApJ, 709, 191, doi: 10.1088/0004-637X/709/1/191
Nayak, O., Meixner, M., Sewiło, M., et al. 2019, ApJ, 877, 135, doi: 10.3847/1538-4357/ab1b38
Oey, M. S., Herrera, C. N., Silich, S., et al. 2017, ApJL, 849, L1, doi: 10.3847/2041-8213/aa9215
Olivier, G. M., Lopez, L. A., Rosen, A. L., et al. 2020, arXiv e-prints, arXiv:2009.10079. https://arxiv.org/abs/2009.10079
Ossenkopf, V., & Henning, T. 1994, a, 291, 943
Paglione, T. A. D., Yam, O., Tosaki, T., & Jackson, J. M. 2004, ApJ, 611, 835, doi: 10.1086/422354
Palouš, J., Wünsch, R., & Tenorio-Tagle, G. 2014, ApJ, 792, 105, doi: 10.1088/0004-637X/792/2/105
Portegies Zwart, S. F., McMillan, S. L. W., & Gieles, M. 2010, ARA&A, 48, 431, doi: 10.1146/annurev-astro-081309-130834
Raskutti, S., Ostriker, E. C., & Skinner, M. A. 2017, ApJ, 850, 112, doi: 10.3847/1538-4357/aa965e
Rekola, R., Richer, M. G., McCall, M. L., et al. 2005, MNRAS, 361, 330, doi: 10.1111/j.1365-2966.2005.09166.x
Rico-Villas, F., Martín-Pintado, J., González-Alfonso, E., Martín, S., & Rivilla, V. M. 2020, MNRAS, 491, 4573, doi: 10.1093/mnras/stz3347
Sakamoto, K., Mao, R.-Q., Matsushita, S., et al. 2011, ApJ, 735, 19, doi: 10.1088/0004-637X/735/1/19
Sakamoto, K., Ho, P. T. P., Iono, D., et al. 2006, ApJ, 636, 685, doi: 10.1086/498075
Schneider, F. R. N., Sana, H., Evans, C. J., et al. 2018, Science, 359, 69, doi: 10.1126/science.aan0106
Schöier, F. L., van der Tak, F. F. S., van Dishoeck, E. F., & Black, J. H. 2005, A&A, 432, 369, doi: 10.1051/0004-6361:20041729
Semenov, D., Henning, T., Helling, C., Ilgner, M., & Sedlmayr, E. 2003, A&A, 410, 611, doi: 10.1051/0004-6361:20031279
Shirley, Y. L. 2015, PASP, 127, 299, doi: 10.1086/680342
Silich, S., Tenorio-Tagle, G., & Rodríguez-González, A. 2004, ApJ, 610, 226, doi: 10.1086/421702
Skinner, M. A., & Ostriker, E. C. 2015, ApJ, 809, 187, doi: 10.1088/0004-637X/809/2/187
Sokal, K. R., Johnson, K. E., Indebetouw, R., & Massey, P. 2016, ApJ, 826, 194, doi: 10.3847/0004-637X/826/2/194
Tang, X. D., Henkel, C., Menten, K. M., et al. 2019, A&A, 629, A6, doi: 10.1051/0004-6361/201935603

The Astropy Collaboration, Price-Whelan, A. M., Sipőcz, B. M., et al. 2018, ArXiv e-prints. https://arxiv.org/abs/1801.02634

Thompson, T. A., & Krumholz, M. R. 2016, MNRAS, 455, 334, doi: 10.1093/mnras/stv2331

Turner, J. L., Beck, S. C., Benford, D. J., et al. 2015, Nature, 519, 331, doi: 10.1038/nature14218

Turner, J. L., Consiglio, S. M., Beck, S. C., et al. 2017, ApJ, 846, 73, doi: 10.3847/1538-4357/aa8669

Turner, J. L., & Ho, P. T. P. 1985, ApJL, 299, L77, doi: 10.1086/184584

Ulvestad, J. S., & Antonucci, R. R. J. 1997, ApJ, 488, 621, doi: 10.1086/304739

van Dishoeck, E. F., & Blake, G. A. 1998, ARA&A, 36, 317, doi: 10.1146/annurev.astro.36.1.317

Vink, J. S., & de Koter, A. 2005, A&A, 442, 587, doi: 10.1051/0004-6361:20052862

Waskom, M., Botvinnik, O., Hobson, P., et al. 2014, Seaborn: V0.5.0 (November 2014), v0.5.0, Zenodo, doi: 10.5281/zenodo.12710

Watson, A. M., Gallagher, J. S., I., Holtzman, J. A., et al. 1996, AJ, 112, 534, doi: 10.1086/118032

Weaver, R., McCray, R., Castor, J., Shapiro, P., & Moore, R. 1977, ApJ, 218, 377, doi: 10.1086/155692

Wünsch, R., Palouš, J., Tenorio-Tagle, G., & Ehlerová, S. 2017, ApJ, 835, 60, doi: 10.3847/1538-4357/835/1/60

Ziurys, L. M., & Turner, B. E. 1986, ApJL, 300, L19, doi: 10.1086/184595

APPENDIX

A. MEASURING OUTFLOW PROPERTIES FROM FITTING THE ABSORPTION FEATURES

For each outflow candidate SSC, we measure important outflow properties based on the $H^{13}CN$ $4-3$ and CS $7-6$ spectra, (Section 3.1, Table 2). Below, we explain how each of these properties is calculated. First, we fit the foreground-removed $H^{13}CN$ $4-3$ and CS $7-6$ spectra with a two-component Gaussian of the form

$$I(V) = I_{max-emis} e^{-(V-V_{max-emis})^2/2\sigma_{emis}^2} + I_{max-abs} e^{-(V-V_{max-abs})^2/2\sigma_{abs}^2} + I_{cont} \quad (A1)$$

with terms to fit the emission, absorption, and continuum components respectively. These fits are shown in Figure 6 as the blue dashed curves. We define the outflow crossing time, which the time it takes a gas parcel to travel from the center of the cluster to r_{SSC} (half the major axis FWHM sizes listed in Table 1) moving at the typical outflow velocity ($V_{max-abs}$) as

$$t_{cross} = \frac{r_{SSC}}{V_{max-abs}}. \quad (A2)$$

This is a lower limit to the outflow age, assuming a constant outflow velocity, since the outflows are observed out to at least r_{SSC} and could be present at larger distances from the cluster. The maximum outflow velocity is defined as

$$V_{out,max} \equiv V_{max-abs} + 2\sigma_{abs}. \quad (A3)$$

We determine the optical depth of the center of the absorption feature where

$$\tau_{max-abs} = -\ln\left(\frac{I_{max-abs}}{I_{cont}}\right). \quad (A4)$$

From there, we calculate the column density in the *lower* state of each molecule following Mangum & Shirley (2015)

$$N_\ell = 16\pi\sqrt{2\ln 2}\left(\frac{\nu_{u\ell}}{c}\right)^2 \sigma_{abs} \frac{\tau_{max-abs}}{A_{u\ell}} \left[e^{h\nu_{u\ell}/kT_{ex}} + 1\right]^{-1} \quad (A5)$$

(combining their equations 29, A1, and A7), where $\nu_{u\ell}$ is the frequency of the transition, c is the speed of light, $A_{u\ell}$ is the Einstein A coefficient for the transition, and T_{ex} is the excitation temperature. By replacing T_ℓ with T_{ex}, we are assuming LTE, which we will assume throughout. We assume $T_{ex} = 130 \pm 56$ K, which is the excitation temperatures found in these clusters (Krieger et al. 2020). The uncertainty is the difference between this value and the excitation temperature measured at lower resolution (74 K; Meier et al. 2015). Our assumption on T_{ex} is a major source of uncertainty in these calculations. We then calculate the column density in the upper state

$$N_u = N_\ell \frac{g_u}{g_\ell} e^{-h\nu_{u\ell}/kT_{ex}} \quad (A6)$$

(e.g. equation 6 of Mangum & Shirley 2015, assuming the upper and lower states have the same density distribution along the line of sight). The total column density of each molecule (e.g. of all energy levels) is

$$N_{mol} = \frac{N_u}{g_u} \mathcal{Z} e^{h\nu_{u\ell}/kT_{ex}} \quad (A7)$$

(e.g. equation 31 Mangum & Shirley 2015), where $\mathcal{Z}$ is the partition function calculated assuming LTE

$$\mathcal{Z} = \sum_i g_i e^{-E_i/kT_{ex}} \quad (A8)$$

where g_i and E_i are the degeneracy and excitation energy of each level i. We calculate $\mathcal{Z}$ assuming LTE up to $i = 19$ for CS and $i = 16$ for $H^{13}CN$[5]. To convert from the column density of each molecule to the column density of H_2 in the outflow ($N_{H_2,outflow}$), we need to know the abundance ratio of each molecule with respect to H_2:

$$N_{H_2,out} = 2\frac{[H_2]}{[mol]} N_{mol} \quad (A9)$$

where the factor of 2 accounts for the redshifted outflowing material, assuming it is the same as the blueshifted component. The abundance ratios vary with environment, so we use those calculated in the center of NGC 253 by Martín et al. (2006), where $[CS]/[H_2] = 5.0 \times 10^{-9}$ and $[H^{13}CN]/[H_2] = 1.2 \times 10^{-10}$. The assumed abundance ratio is another large source of uncertainty in our measurements and can vary substantially by environment (e.g. van Dishoeck & Blake 1998, and references therein). We take a order-of-magnitude uncertainty on the abundance fractions, which limits subsequent calculations to order-of-magnitude precision as well (see the discussion in Section 3.1.1).

To calculate the H_2 mass along the line of sight,

$$M_{H_2,out} = 4\Sigma_{H_2,out} A = 4 m_{H_2} N_{H_2,out} A \quad (A10)$$

where A is the area of the source measured from the continuum (Table 2), m_{H_2} is the mass of a hydrogen molecule, and the factor of 4 converts the projected area to a sphere.

[5] Level population data are from https://www.astro.umd.edu/rareas/lma/lgm/properties/cs.pdf for CS and https://www.astro.umd.edu/rareas/lma/lgm/properties/h13cn.pdf for $H^{13}CN$.

From the mass in the outflow and the crossing time, we calculate the mass outflow rate ($\dot{M}_{H_2,out}$) where

$$\dot{M}_{H_2,out} = \frac{M_{H_2,out}}{t_{cross}}. \quad (A11)$$

From the total gas mass of the cluster (Leroy et al. 2018) and the mass outflow rate, we calculate the gas-removal time, or the time it would take to expel all of the gas in the cluster at the current mass outflow rate:

$$t_{remove-gas} = \frac{M_{H_2,tot}}{\dot{M}_{H_2,out}}. \quad (A12)$$

The timescale assumes that the mass outflow rate is constant with time, which is likely not the case (e.g. Kim et al. 2018). The momentum injected into the environment normalized by the stellar mass (M_*) by the outflow is

$$\frac{p_r}{M_*} = \frac{\sqrt{3} V_{max-abs} M_{H_2,out}}{M_*} \quad (A13)$$

assuming spherical symmetry (Leroy et al. 2018). We assume the SSC stellar masses reported by Leroy et al. (2018). Although some of the SSCs break up into multiple components at this higher resolution, there is a main, brightest cluster which we will assume retains the majority of the stellar mass. This uncertainty in the stellar mass is likely smaller than the other sources of uncertainty already discussed in these calculations. The kinetic energy in the outflow is

$$E_k = \frac{1}{2} M_{H_2,out} V^2_{max-abs}. \quad (A14)$$

Values calculated using CS $7-6$ and $H^{13}CN$ $4-3$ for each outflow candidate are listed in Table 2 along with the propagated uncertainties.

B. OUTFLOW MODELING DETAILS

We perform simple radiative transfer modeling of the source with varying outflow geometries and input physical parameters to constrain the outflow opening angles and orientations as described in Section 3.2.

To set up the model, we define a three-dimensional grid that is 65 (= 2^4+1) pixels in each dimension; we refer to this grid as the simulated box. The physical scale of the box is such that the length of each size is $4 \times r_{SSC}$, or twice the diameter of the SSC to be modeled. Every pixel in the box is given a fourth dimension, corresponding to the spectral axis (in terms of frequency or velocity, which we use interchangeably here). The spectral axis has 129 (= 2^7+1) channels. The velocity range of the spectral axis and hence the spectral resolution of the model is defined adaptively for each model to maximize the number of channels over the emission and absorption features. The spectral axis is centered

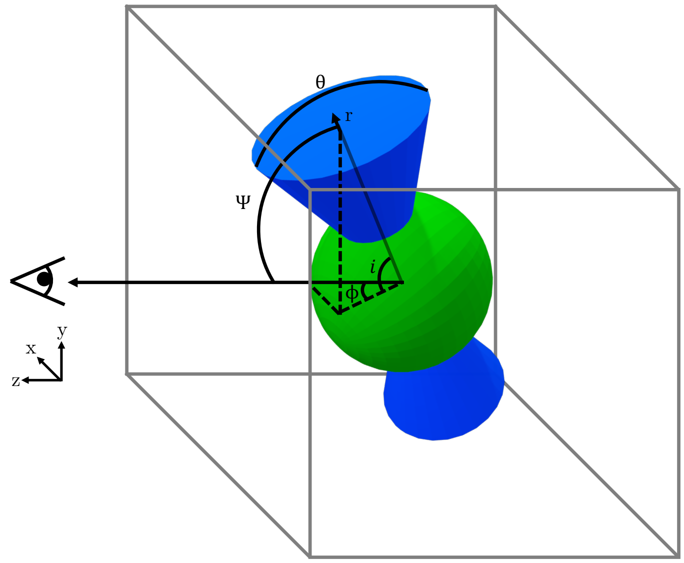

Figure B1. An example outflow, in the style of Figure 8; for clarity, the ambient gas is not shown. The simulated box is shown in gray. The orientation angle definitions are marked, where θ is the outflow opening angle and Ψ is the orientation angle to the line of sight measured from the center of the outflow cone with components i and ϕ to the x- and y-axis respectively.

on zero velocity (the rest frequency of the line to be modeled) and spans $\pm 4\sqrt{V^2_{max-abs} + \Delta V^2_{out,FWHM}}$, where $V_{max-abs}$ and $\Delta V_{out,FWHM}$ are the outflow velocity and FWHM outflow velocity dispersion input into the model. This is done to optimize the velocity resolution over the velocities relevant for the cluster and outflow as opposed to picking a fixed velocity range. This is shown most clearly in Figure 7, where the portions of the spectra within the vertical red lines show the velocities actually modeled and the thin lines are extrapolations.

Once the four-dimensional box is defined, the three physical components representing the cluster and outflow are constructed. It is helpful to define coordinates related to the simulated box in cartesian coordinates, whereas coordinates pertaining to the cluster and outflow are in spherical coordinates, as shown in Figure B1. As described in Section 3.2, the three components of the system are:

1. Dust continuum component: Shown in green in Figures 7, 8, B1, and B2 this component is a sphere with $r = r_{SSC}$ and a constant (in space and velocity) temperature (T_{cont}). The optical depth is a maximum ($\tau_{cont,max}$) at the center, then decreases like a Gaussian with FWHM = $2 \times r_{SSC}$, so that the continuum source is semi-transparent. The temperature and optical depth are set to zero for $r > r_{SSC}$.

2. Hot gas: Shown in yellow in Figures 7 and B2 (and encompassed within the green sphere in Figures 8 and B1), this spherical component is required to repro-

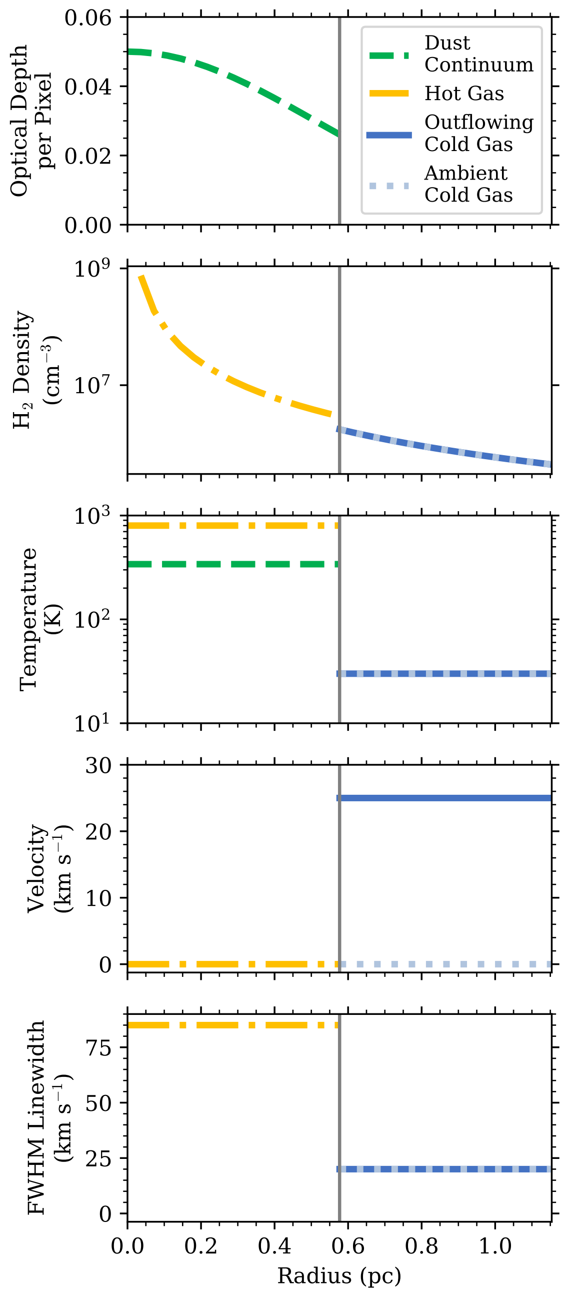

Figure B2. Radial profiles of the input parameters to the modeling for the dust continuum (green dashed), hot gas (gold dash-dotted), outflowing cold gas (blue solid), and the ambient cold gas (light blue dotted) as described in Section 3.2. For the dust continuum, the optical depth per pixel is specified, whereas for the other components, the H_2 density per pixel is specified. For the ambient cold gas, input parameters are identical to the outflowing cold gas except for the velocity. Cold gas inside the outflow cones has the properties of the outflowing cold gas, whereas cold gas outside the outflow cones has the properties of the ambient cold gas. The vertical gray line marks $r_{\rm SSC}$ which is the boundary between the cluster (e.g. continuum and hot gas components) and the cold gas components (outflowing or ambient). These input parameters are scaled to the best-fit spherical model for the CS 7 − 6 line in SSC 14 (Table 3).

duce the strong emission component of the P-Cygni profiles. This component has a hot gas temperature ($T_{\rm hot}$), a central H_2 volume density ($n_{\rm hot}$), and a velocity dispersion ($\Delta V_{\rm hot,FWHM}$). $T_{\rm hot}$ is constant (spatially) for $r \leq r_{\rm SSC}$, and is set to zero outside. The density falls off $\propto r^{-2}$ from the center, and is set to zero for $r > r_{\rm SSC}$. The line is centered on zero velocity along the spectral axis, and the Gaussian linewidth is given by $\Delta V_{\rm hot,FWHM}/2.355$.

3. Cold, outflowing gas: Shown in dark blue in Figures 7, 8, B1, and B2 this is the outflow component which produces the absorption features. This component is defined by a gas temperature ($T_{\rm out}$), a maximum H_2 volume density ($n_{\rm out}$), a constant outflow velocity ($V_{\rm out}$), a velocity dispersion ($\Delta V_{\rm out,FWHM}$), and opening angle (θ), and an orientation to the line of sight (Ψ). The gas temperature is constant (spatially) within this component and is set to zero for $r < r_{\rm SSC}$. The density is a maximum at $r = r_{\rm SSC}$ and deceases $\propto r^{-2}$ until the edges of the box; the density is set to zero for $r < r_{\rm SSC}$. The line is centered on along the frequency axis at $V_{\rm outflow}$, and the Gaussian linewidth is given by $\Delta V_{\rm out,FWHM}$. Since the outflow velocity is constant and the density $\propto r^{-2}$, the outflow conserves energy and momentum. The outflow cones are masked to the given opening angle (θ) and rotated to the given orientation from the line of sight (Ψ) (Figure B1). For outflows with $\theta < 180°$, the outflowing gas component outside the outflow cones is replaced by an ambient gas component (shown in light blue in Figures 8 and B2), which has the same properties as the outflowing gas but with $V_{\rm out} = 0$. We refer to these together simply as the "cold" component.

The optical depths of the hot and cold (outflowing and ambient) gas are needed at every pixel and as a function of frequency ($\tau_{\nu,\rm hot}$ and $\tau_{\nu,\rm outflow}$ respectively) for the radiative transfer. For simplicity in the following equations, we will drop the "hot" and "cold" subscripts since the calculations are the same for both components. First, we calculate the intrinsic line shape assuming Doppler broadening is dominant

$$\phi_\nu = \frac{1}{\sqrt{\pi}\nu_{u\ell}}\frac{c}{b}e^{-V^2/b^2} \tag{B15}$$

where $b \equiv \sqrt{2}\sigma_V = \frac{\Delta V_{\rm FWHM}}{2\sqrt{\ln 2}}$, $\nu_{u\ell}$ is the rest frequency of the transition being modeled, and V is the velocity along the spectral axis (with $V = 0$ corresponding to $\nu = \nu_{u\ell}$) and where $\int \phi_\nu d\nu = 1$ (Draine 2011). The absorption cross section is

$$\sigma_{\ell u}(\nu) = \frac{g_u}{g_\ell}\frac{c^2}{8\pi\nu_{u\ell}^2}A_{u\ell}\phi_\nu \tag{B16}$$

where g_u and g_ℓ are the upper and lower level degeneracies and $A_{u\ell}$ is the Einstein A value of the transition[5]

(Draine 2011). Given the H_2 number density at every pixel ($n_{H_2}(x,y,z)$), the number density in the lower state of the modeled transition is

$$n_\ell(x,y,z) = \frac{[\mathrm{mol}]}{[\mathrm{H_2}]}\frac{g_\ell}{\mathcal{Z}} e^{-T_\ell/T} n_{\mathrm{H_2}}(x,y,z) \tag{B17}$$

where $\frac{[\mathrm{mol}]}{[\mathrm{H_2}]}$ is the fractional abundance of the molecule being modeled with respect to H_2, $\mathcal{Z}$ is the partition function (Equation A8), $T_\ell \equiv E_\ell/k$ is the excitation energy of the lower energy state, and T is the input temperature of the gas. The absorption coefficient is then

$$\kappa_\nu(x,y,z) = n_\ell(x,y,z)\sigma_{\ell u}(\nu)\left(1-e^{-k\nu/kT}\right) \tag{B18}$$

(Draine 2011). Finally, the optical depth of each pixel and as a function of frequency is

$$\Delta\tau_\nu(x,y,z) = \kappa_\nu(x,y,z)\Delta z \tag{B19}$$

where Δz is the size of each pixel in the z direction (though in this simulation the pixels are equal size in all spatial dimensions).

For each component—now also including the continuum component— the intensity (expressed in Rayleigh-Jeans brightness temperature units) at every pixel and as a function of frequency is

$$\Delta T_\nu(x,y,z) = T\left[1-e^{-\Delta\tau_\nu(x,y,z)}\right]. \tag{B20}$$

We perform the radiative transfer along the line of sight from the back of the box to the front (e.g. along the $+z$-axis):

$$T_\nu(x,y,z_i) = T_\nu(x,y,z_{i+1})e^{-\sum_{\mathrm{comp}}\Delta\tau_\nu(x,y,z_i)} + \sum_{\mathrm{comp}}\Delta T_\nu(x,y,z_i) \tag{B21}$$

where z_i denotes an individual step along the z-axis and $\sum_{\mathrm{comp}}$ means a sum over the dust continuum, hot gas, and cold (outflowing and ambient) gas components.

The observed spectra are averaged over the FWHM continuum source size. To best compare with the observed spectra, we mask the simulated box of $T_\nu(x,y,z)$ to a cylinder along the z-axis with $r = r_{\mathrm{SSC}}$ as shown in Figure 8, setting pixels outside this region equal to zero. The final modeled spectrum is

$$T_\nu = \frac{1}{N_{\mathrm{pix}}}\sum_{x,y} T_\nu(x,y,z=z_{\mathrm{max}}) \tag{B22}$$

where $z = z_{\mathrm{max}}$ denotes the slice (in the xy plane) at the front of the box and N_{pix} is the number of non-masked pixels in that slice. The best-fitting modeled spectra are shown in red in Figure 6.

There are degeneracies between input parameters. The observed continuum level is a combination of the intrinsic continuum temperature (T_{cont}) and the continuum optical depth (τ_{cont}); a higher τ_{cont} with a lower T_{cont} can produce the same fit as a lower τ_{cont} with a higher T_{cont}. The temperature and density of the hot gas component (T_{hot} and n_{hot}) are linked in a similar way. More, a lower τ_{cont} means less of the hot gas and redshifted outflow are attenuated, and so lower T_{hot} and n_{hot} values are required. These degeneracies, especially with regards to the density, lead to a very uncertain total mass for the modeled cluster. The outflow parameters, however, are more robust. The gas temperature in the outflow (T_{out}) is linked to the density in the outflow (n_{out}), but are not as degenerate as for the hot gas component. For absorption, the observed brightness temperature cannot be less than the given T_{out}, even for an arbitrarily high density. That is, the observed temperature at maximum absorption sets the maximum possible T_{out}. For these reasons, though we report all input parameters for the best-fitting models, we only report derived parameters for the outflow in Table 3.